



Cosmic Sands: The Origin of Dusty, Star-forming Galaxies in the Epoch of Reionization

Sidney Lower¹ , Desika Narayanan^{1,2,3} , Qi Li⁴ , and Romeel Davé^{5,6} ¹ Department of Astronomy, University of Florida, 211 Bryant Space Science Center, Gainesville, FL 32611, USA² University of Florida Informatics Institute, 432 Newell Drive, CISE Bldg E251 Gainesville, FL 32611, US³ Cosmic Dawn Centre at the Niels Bohr Institute, University of Copenhagen and DTU-Space, Technical University of Denmark⁴ Max-Planck-Institut für Astrophysik, Karl-Schwarzschild-Str. 1, Garching b. München D-85741, Germany⁵ Institute for Astronomy, Royal Observatory, University of Edinburgh, Edinburgh, EH9 3HJ, UK⁶ Department of Physics and Astronomy, University of the Western Cape, Bellville, 7535, South Africa

Received 2022 December 5; revised 2023 April 19; accepted 2023 April 21; published 2023 June 13

Abstract

We present the Cosmic Sands suite of cosmological zoom-in simulations based on the SIMBA galaxy formation model in order to study the buildup of the first massive and dusty galaxies in the early universe. Residing in the most massive halos, we find that the compact proto-massive galaxies undergo nearly continuous mergers with smaller subhalos, boosting star formation rates (SFRs) and the buildup of stellar mass. The galaxies are already appreciably chemically evolved by $z=7$, with modeled dust masses comparable to those inferred from observations in the same epoch, except for the most extreme systems. We track gas accretion onto the galaxies to understand how extreme SFRs can be sustained by these early systems. We find that smooth gas accretion can maintain SFRs above $250 M_{\odot} \text{ yr}^{-1}$, but to achieve SFRs that boost galaxies well above the main sequence, a larger perturbation like a gas-rich major merger is necessary to trigger a starburst episode. Post-processing the Cosmic Sands simulations with dust RT, we find that, while the infrared luminosities of the most-dust-rich galaxies are comparable to local ULIRGs, they are substantially dimmer than classical $z=2$ submillimeter galaxies. We end with a discussion on the possible reasons for this discrepancy at the highest masses and the future work we intend to carry out to study the chemical enrichment of the earliest dusty galaxies.

Unified Astronomy Thesaurus concepts: [Galaxies \(573\)](#); [Hydrodynamical simulations \(767\)](#); [Ultraluminous infrared galaxies \(1735\)](#); [Starburst galaxies \(1570\)](#)

1. Introduction

By the time the universe was 1 billion years old, the dawn of galaxy formation was already well underway. The processes that govern the formation of the most massive galaxies during this time are still relatively uncertain. From a theoretical standpoint, studying these processes requires connecting physics across several orders of magnitude in spatial (as well as mass and temporal) scales, from star formation on subparsec scales to galactic outflows and the baryon cycle on kiloparsec scales to galaxy–galaxy interactions over megaparsec scales. Modeling the formation of early massive galaxies has been a numerical challenge for several decades. The first attempts with semianalytic models focused on explaining the origin of high-redshift submillimeter galaxies (SMGs), Lyman-break galaxies (LBGs), and quasars (Guiderdoni et al. 1998; Devriendt & Guiderdoni 2000; Somerville et al. 2001; Granato et al. 2004; Baugh et al. 2005; Swinbank et al. 2008) individually. Later, more robust galaxy formation frameworks were implemented that evolved these populations together (Fontanot et al. 2007; Somerville et al. 2012; Valiante et al. 2014; Lacey et al. 2016; Béthermin et al. 2017; Popping et al. 2017; Lagos et al. 2019; Triani et al. 2020; Hutter et al. 2021; Trinca et al. 2022) and used hydrodynamic models coupled with dust radiative transfer (RT) to produce high- z populations of massive galaxies with realistic growth histories and radiative properties (Davé et al. 2010; Narayanan et al. 2010a, 2010b; Shimizu et al. 2012;

Hayward et al. 2013b; Narayanan et al. 2015; Poole et al. 2016; McAlpine et al. 2019; Kim et al. 2019; Lovell et al. 2021c, 2021b).

Of particular interest is the population of infrared luminous SMGs that have been detected as early as redshift $z=6.9$ (Marrone et al. 2018). These systems are some of the most extreme in the universe, with stellar masses estimated to be comparable to the Milky Way that formed in less than 1 billion years after the Big Bang. Their intense infrared luminosities, comparable to those of local ULIRG galaxies, are thought to be the result of massive dust reservoirs heated by compact starbursts (Ginolfi et al. 2019). The rarity of these systems makes them difficult to study, with number counts estimated to be $<10/\text{deg}^2$ past $z=6$ (Wardlow et al. 2011; Simpson et al. 2014; Ivison et al. 2016; Reuter et al. 2020; Zavala et al. 2021). Given their rareness, they are not perfectly traced by dark-matter overdensities (Chapman et al. 2009; Miller et al. 2015). Even with their intrinsic rarity, these extreme systems were the first insights into early galaxy formation, challenging theoretical models that attempted to explain their rapid buildup and stellar and dust masses.

For instance the onset and nature of star formation and the impact of local and global feedback mechanisms remain relatively uncertain. Similarly, the question of how these same galaxies build up dust reservoirs in excess of $10^7 M_{\odot}$ is also difficult to reconcile with current theory. Estimates for dust yields from Type II supernovae (SNe) can explain the dust masses for galaxies at $z > 6$ only if the destruction rates are negligible (Mancini et al. 2015; Michałowski 2015; Burgarella et al. 2020), as chemical enrichment from evolved asymptotic giant branch (AGB) stars is negligible at these redshifts (see Valiante et al. 2009 for a contrasting view).

With the additional constraints of “normal” dusty, star-forming galaxies (DSFGs) at $z > 5 - 6$ from ALMA large program (e.g., REBELs, Bouwens et al. 2022; ALPINE, Le Fèvre et al. 2020), we are beginning to understand that even relatively small galaxies have sizeable dust mass reservoirs, and that early dust enrichment is not just a characteristic of the most extreme systems. Establishing how and when the buildup of both stellar and dust masses occurs is necessary to understand the origin of the first infrared luminous galaxies.

Two recent works have significantly advanced our understanding of early galaxy formation in a cosmological context: the FirstLight project (Ceverino et al. 2017), a large suite of hydrodynamic zoom-in simulations, successfully reproduced observed galaxy stellar mass and ultraviolet (UV) luminosity functions and the star-forming main-sequence relation out to redshift $z = 10$. The FLARES project, based on EAGLE physics (Crain et al. 2015; Schaller et al. 2015; Schaye et al. 2015; McAlpine et al. 2016) and implementing a novel simulation scheme to model overdensities in the Epoch of Reionization (EoR), has also successfully formed galaxies with physical and photometric properties consistent with observations out to redshift $z = 10$ (Lovell et al. 2021c; Vijayan et al. 2021). This said, neither the FirstLight nor FLARES projects are able to produce galaxies during the EoR that span of the range of colors and masses inferred by current constraints, especially the most extreme systems observed to date (e.g., Watson et al. 2015; Marrone et al. 2018; Hashimoto et al. 2019; Reuter et al. 2020; Endsley et al. 2022), potentially due to a lack of models for the formation and evolution of dust.

Aiming to place infrared bright galaxies into the context of galaxy evolution, Narayanan et al. (2015) presented a theory for the evolution of SMGs at intermediate redshifts ($1 < z < 2$). These galaxies experience gas-rich minor mergers with small subhalos that trigger bursts of star formation, resulting in a compact stellar core with extended long-lived infrared emission. Lovell et al. (2021b) extended this framework into a cosmological context by nearly reproducing observed SMG number counts with the SIMBA hydrodynamical simulation, echoing the findings from Narayanan et al. (2015) that infrared luminous phases are a natural consequence of massive galaxy evolution. However, it is not obvious if this framework extends out to high redshift ($z > 6$). Indeed, neither Narayanan et al. (2015) nor Lovell et al. (2021b) modeled a sufficiently large volume with high enough resolution to form DSFGs at $z > 6$.

To this end, we present the Cosmic Sands sample of dusty galaxies, occupying an effective volume of $(0.5 \times 100 \text{ Mpc})^3$ and modeled with the SIMBA galaxy formation suite (Davé et al. 2019) that includes well-constrained models for star formation, stellar feedback, black hole (BH) growth and active galactic nuclei (AGN) feedback, and dust production growth, and destruction. These high-resolution zoom-in simulations are among the first to couple stellar evolution and dust growth, building off the analysis and findings of works like Graziani et al. (2020), Di Cesare et al. (2023), McKinnon et al. (2016, 2017), Aoyama et al. (2018), Aoyama et al. (2020), Choban et al. (2022), Granato et al. (2021), and Lewis et al. (2023), to enable detailed studies into the formation pathways of early massive galaxies, with a focus on modeling the most extreme star-forming galaxies in the EoR. In this paper, we aim to understand the mechanisms through which DSFGs build up their extensive amounts of gas, stellar, and dust masses in the

first billion years of cosmic history, focusing on their formation pathways and the drivers of their early star formation.

In what follows, we outline the galaxy formation model SIMBA and the post-processing RT code POWDERDAY in Section 2, the physical properties of the galaxies and comparisons to observations from the literature in Section 3, and answer the question “What sustains the intense star formation rates (SFRs) observed in high- z DSFGs?” in Section 4. Finally, in Section 5, we discuss to what degree our Cosmic Sands galaxies match the observed properties of high- z galaxies as well as the fundamental uncertainties in our model.

2. Numerical Methods

2.1. The SIMBA Galaxy Formation Model

Our massive galaxy sample is generated from the SIMBA galaxy formation model. SIMBA (Davé et al. 2019) is based on the GIZMO gravity and hydrodynamics code (Hopkins 2015) and includes models describing heating and cooling, star formation, chemical enrichment, feedback from stellar winds, dust production and growth, and BH accretion and feedback. We briefly summarize the key aspects of each model.

Star formation occurs in dense molecular clouds, with rates governed by the density of H_2 divided by the local dynamical timescale. The H_2 fraction is modeled with the subgrid prescription of Krumholz & Gnedin (2011) depending on the gas-phase metallicity and local gas column density. We impose a minimum density limit ($n_{\text{H}} \geq 0.13 \text{ cm}^{-3}$) below which stars do not form.

SIMBA uses the GRACKLE-3 library (Smith et al. 2017) to model radiative cooling and photoionization heating including a self-consistent model for self-shielding based on Rahmati et al. (2013). The chemical enrichment model tracks 11 elements from Type Ia and II SNe and AGB stars with yields following Nomoto et al. (2006), Iwamoto et al. (1999), and Oppenheimer & Davé (2006), respectively.

Stellar feedback is implemented with contributions from Type II SNe, radiation pressure, and stellar winds. The two-component stellar winds adopt the mass-loading factor scaling from FIRE (Anglés-Alcázar et al. 2017) with wind velocities given by Muratov et al. (2015). Metal-enriched winds extract metals from nearby particles to represent the local enrichment by the SNe driving the wind. Feedback via active AGN is implemented as a two-phase jet (low accretion rate) and radiative (high accretion rate) model. Thermal energy is injected into the surrounding interstellar medium (ISM) at high accretion rates, while BH-driven winds are produced at low accretion rates.

Dust is modeled self-consistently, and on the fly in the galaxy evolution simulations. Following the fiducial models of Li et al. (2019), based on the prescription of Dwek (1998), Popping et al. (2017), dust is produced by the condensation of metals ejected from Type II SNe and AGB stars, and is allowed to grow and erode depending on local ISM temperature, density, and shocks from Type I and Type II SNe. Dust production from stellar sources occurs following the models of Ferrarotti & Gail (2006) for AGB stars and Bianchi & Schneider (2007) for SNe, with condensation efficiencies of $\delta_{\text{dust}}^{\text{AGB}} = 0.2$, and $\delta_{\text{dust}}^{\text{SN II}} = 0.15$, which control the fraction of ejected metals that are locked into dust.

Dust growth in the ISM occurs via accretion of metals onto the seeded dust grains:

$$\left(\frac{dM_d}{dt}\right)_{\text{grow}} = \left(1 - \frac{M_d}{M_{\text{metal}}}\right) \left(\frac{M_d}{\tau_{\text{accr}}}\right), \quad (1)$$

where M_{metal} is the total mass of dust and local gas-phase metals. The accretion rate, τ_{accr} , is governed by the local gas density, temperature, and metallicity, with the reference density scaled by the ratio of the median ISM density in the zooms to the median ISM density in the lower-resolution 100 Mpc h^{-1} SIMBA box (Li et al. 2019). At solar metallicity, the gas with densities of $\rho_g = 500$ H atoms cm^{-3} and temperatures of $T_f = 20$ K has dust growth timescales of $\tau_{\text{grow}} = 10$ Myr.

Lastly, dust grains are eroded via thermal sputtering and can be destroyed entirely by SNe shocks. The sputtering timescale depends on the gas density and temperature, with the sputtering rate flattening above temperatures of 2×10^6 K. In hot diffuse gas ($n \sim 6 \times 10^{-4}$ cm^{-3}), the sputtering rate is ~ 0.3 Gyr. The corresponding change in dust mass via sputtering follows

$$\left(\frac{dM_d}{dt}\right)_{\text{sp}} = -\frac{M_d}{\tau_{\text{sp}}/3}. \quad (2)$$

SNe shocks are not directly modeled; thus we implement an SNe destruction mode with a timescale dependent on the mass of gas shocked to velocities of at least 100 km s^{-1} with a fixed grain destruction efficiency of 0.3 following McKee (1989). The rate of change in dust mass due to SN destruction is given by the total dust mass scaled by the shocked gas mass and the local SN II rate. In hot winds, during star formation, and in any gas that is impacted by AGN feedback, dust is assumed to be completely destroyed.

2.2. Zoom-in Technique

We generate our suite of massive galaxies using a zoom-in technique that enables our simulations to be generated at higher-mass resolutions, and thus finer detail, while still maintaining the cosmological scale of a larger box. We do this by creating 32 dark-matter-only simulations with initial conditions set by MUSIC (Hahn & Abel 2011). Each simulation is 25 Mpc^3 in volume and evolved from $z = 249$, to $z = 0$. We then select the largest halo from each box at redshift $z = 2$ using CAESAR (Thompson 2014) and construct an ellipsoidal mask around all particles within $2.5 \times$ the radius of the maximum distance dark-matter particle in the halo. This is defined as the Lagrangian high-resolution region to be resimulated at a higher resolution with baryon physics included. The zoom-ins reach an effective mass resolution of $m_{\text{baryon}} \sim 2.9 \times 10^5 M_{\odot}$ for particles within the zoom-in radius. We identify galaxies within each halo again using CAESAR with a 6D friends-of-friends galaxy finder based on the number of bound stellar particles in a system (a minimum of 32 stellar particles defines a galaxy).

The zoom-ins are initialized at $z = 249$, and snapshots are saved in intervals of 30 Myr beginning at redshift $z_{\text{init}} = 10$, with a select subsample of halos saved at earlier times ($z_{\text{init}} = 25$) and at finer time resolution ($\Delta t = 15$ Myr). In total, our 32 zoom-in simulations represent an effective volume of $4 \times 50 \text{ Mpc}^3$. We note, however, that the use of several 25 $\text{Mpc} h^{-1}$ boxes will not capture the largest perturbations and may be missing some of the larger scale structure that would be

present in a 100 $\text{Mpc} h^{-1}$ box, thus slightly biasing our sample against the highest-mass halos.

2.3. 3D Dust Radiative Transfer

We post-process the simulated galaxies with 3D dust RT to generate UV–far-infrared (FIR) SEDs for each massive galaxy. We use the RT code POWDERDAY⁷ (Narayanan et al. 2020) to construct the synthetic SEDs by first generating with FSPS (Conroy et al. 2009; Conroy & Gunn 2010) the dust-free SEDs for the star particles within each cell using the stellar ages and metallicities as returned from the cosmological simulations. For these, we assume a Kroupa (2002) stellar initial mass function (IMF) and the MIST stellar isochrones (Choi et al. 2016; Dotter 2016). These FSPS stellar SEDs are then propagated through the dusty ISM. The diffuse dust content is derived from the on-the-fly self-consistent model of Li et al. (2019). As SIMBA contains a “passive” dust model, with a single grain size (0.1 μm), the dust is assumed to have extinction properties following the carbonaceous and silicate mix of Draine & Li (2007). This model includes the Weingartner & Draine (2001) size distribution and the Draine (2003) renormalization relative to hydrogen. We assume $R_V \equiv A_V/E(B - V) = 3.15$.

Polycyclic aromatic hydrocarbons (PAHs) are included following the Robitaille et al. (2012) model in which PAHs are assumed to occupy a constant fraction of the dust mass (here, modeled as grains with size $a < 20$ Å) and occupying 5.86% of the dust mass. The dust emissivities follow the Draine & Li (2007) model, although they are parameterized in terms of the mean intensity absorbed by grains, rather than the average interstellar radiation field as in the original Draine & Li model.

The RT propagates through the dusty ISM in a Monte Carlo fashion using HYPERION (Robitaille 2011), which follows the Lucy (1999) algorithm in order to determine the equilibrium dust temperature in each cell. For imaging, we propagate 10^8 photon packets, and for SEDs we use 10^6 . Gas particles are smoothed onto a grid, which is refined to a maximum of 16 particles in each cell, with a minimum cell size ranging between 0.05–0.2 kpc. We iterate until the energy absorbed by 99% of the cells has changed by less than 1%.

We perform RT on snapshots for several viewing angles with a fixed aperture radius of 50 kpc, roughly equal to the beam size of the SCUBA-2 camera on JCMT at 850 μm for $z > 2$ (Geach et al. 2017), following the methodology of Lovell et al. (2021b). As the simulated galaxies are relatively compact (most have half-mass radii < 3 kpc, with notable exceptions during periods of galaxy–galaxy interactions, which happen on scales of 10–40 kpc), we chose a large aperture to capture this emission. In doing so, we explicitly include emission not just from the FOF identified galaxies but also the surrounding halo.

We also note that this field of view is comparable to that of ALMA in band (7), assuming a relatively compact configuration; while ALMA would measure the same integrated flux over the entire field of view as JCMT, the angular resolution of the image would be much improved.

3. Cosmic Sands: Massive, Dusty Galaxies at Cosmic Dawn

3.1. Sample Overview and Observational Constraints

In Figure 1, we plot the distribution of masses for the halos and galaxies at redshift $z = 6.7$ as well as the stellar mass—halo

⁷ <https://github.com/dnarayanan/powderday>

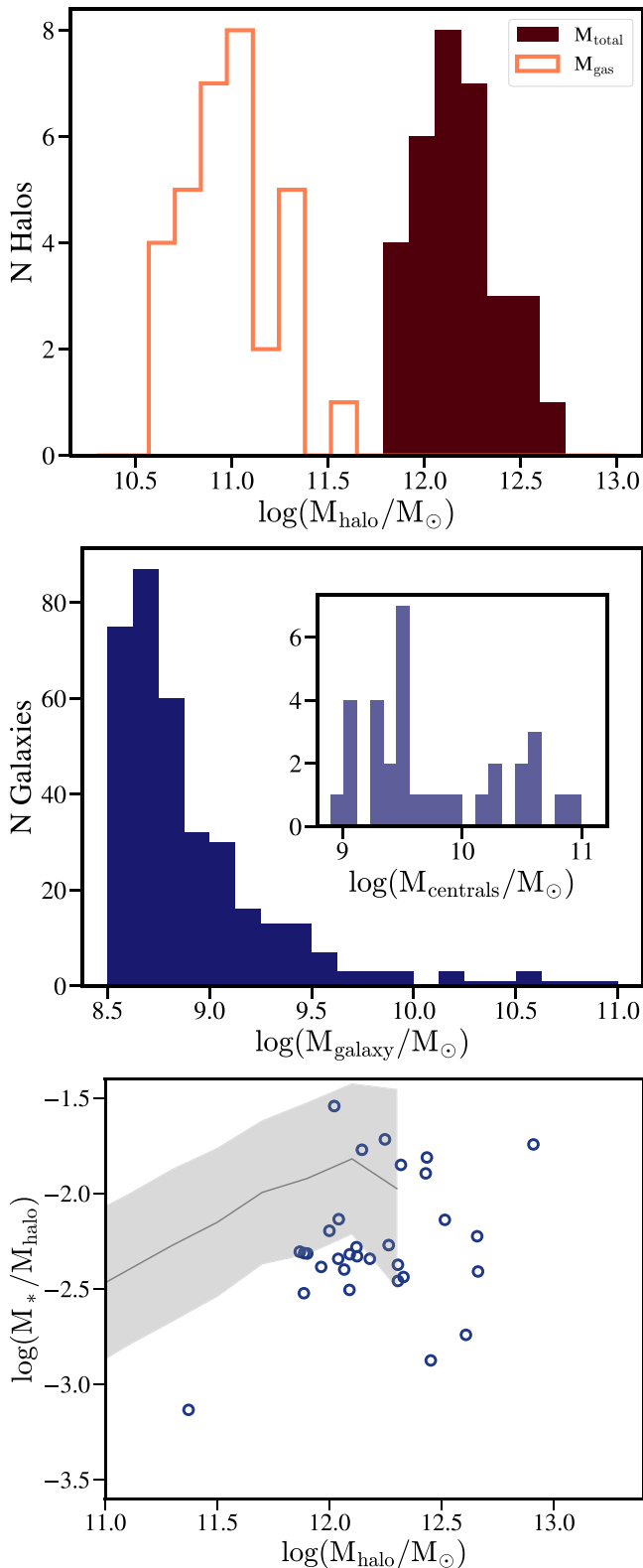


Figure 1. Top: distribution of all Cosmic Sands halos at redshift $z = 6.7$. The filled histogram shows the distribution of total (gas + dark matter + stars) halo mass while the outlined histogram shows only the halo gas mass distribution. Middle: mass (gas + stars) distribution for all galaxies residing in the halos in the top panel. The inset plot highlights the central galaxies, defined as the galaxy residing in the minimum potential well. Bottom: M_* - M_{halo} relation at $z = 6.7$, where the stellar mass is the sum of all subhalos, and the halo mass is the total (gas + dark matter + stellar) mass. The gray curve and shaded region show the relation from the Universe Machine (Behroozi et al. 2019).

mass relation. The halos span an order of magnitude in gas masses, which drives the diversity in central galaxy masses; as we will discuss below, the gas accretion and SFRs are largely set by the halo gas mass alone. While we derive the initial conditions for our zoom-in simulations from a series of dark-matter-only simulations that, in aggregate, encompass an effective volume of $4 \times 50 \text{ Mpc}^3$, in practice, our models are not necessarily representative of this volume since we pick only the most massive halo within each subvolume to zoom in on.

By redshift 6.7, 9 halos have produced central galaxies with a stellar mass above $10^{10} M_{\odot}$. We choose this epoch to compare our simulated massive galaxies with observations of high- z galaxies around the same redshift ($z > 6.4$) as we are primarily interested in the first billion years of evolution. These observations include galaxies from the REBELS program (Bouwens et al. 2022; Fudamoto et al. 2021; Ferrara et al. 2022; Sommovigo et al. 2022; Dayal et al. 2022; Topping et al. 2022), the South Pole Telescope (SPT)-selected DSFG catalog (Vieira et al. 2013; Marrone et al. 2018; Reuter et al. 2020), and a selection of other galaxies at similar epochs, including both dusty starbursts and LBGs: A1689-zD1 (Watson et al. 2015; Knudsen et al. 2017; Bakx et al. 2021), A2744_YD4 (Laporte et al. 2017), B14-65666 (Hashimoto et al. 2019), COS-87259 (Endsley et al. 2022), and HFLS3 (Riechers et al. 2013; Cooray et al. 2014). We have selected galaxies that have robust measurements for redshift, stellar mass ($\gtrsim 10^9$), SFR, and dust mass for the most uniform means of comparison for the simulated galaxies.

In Figure 2, we plot the SFRs and stellar masses of the simulated galaxies and the selected galaxies from the literature. For our zoom-in simulations, the infrared luminosities are calculated from the POWDERDAY mock SEDs, integrated from 8–1000 μm . The physical properties are measured from the gas and star particles within the POWDERDAY aperture, to ensure that the masses, SFRs, and luminosities are self-consistent with one another. This is in contrast to Figure 1, in which the masses are calculated from only the particles that are bound to the central galaxy as determined from the CAESAR friends-of-friends algorithm. Thus, there may be some minor but intentional inconsistencies between Figures 1 and 2, which do not impact our analysis. The zoom-in galaxies span a wide range of stellar masses and SFRs averaged over 50 Myr, ranging from $\log(M_*/M_{\odot}) = 3.7 \times 10^8$, to $\log(M_*/M_{\odot}) = 7.4 \times 10^{10}$, and $\text{SFR} = 1.46 M_{\odot} \text{ yr}^{-1}$, to $\text{SFR} = 937 M_{\odot} \text{ yr}^{-1}$. These values encompass the range of high- z galaxies from the literature and generally lie along the star-forming main-sequence relation for $z = 6.7$.

We note that our sample of zoom-in simulations are not necessarily a representative sample of massive galaxies in the first billion years but rather an illustrative one; the sample provides opportunities to study the difference modes of DSFG evolution. For that reason, we do not compare number counts or population statistics to observations from the literature. In what follows, we present the physical properties of our massive galaxies as well as mock spectral energy distributions (SEDs) and imaging generated by our POWDERDAY RT.

3.2. Galaxy Physical Properties

In less than one billion years, nearly a third of our massive galaxy sample has reached a stellar mass of $10^{10} M_{\odot}$ or larger. In this section, we overview the star formation and dust mass

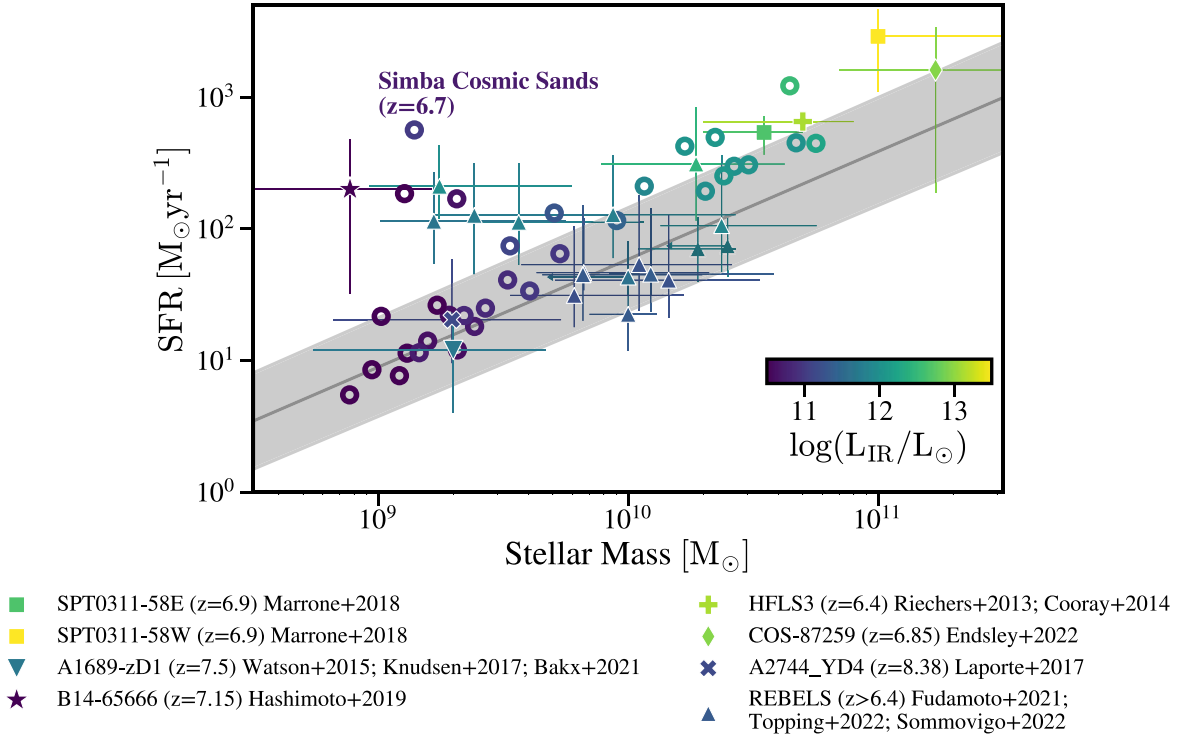


Figure 2. SFR as a function of stellar mass for our zoom-in simulations (colored circles) and observations (various colored symbols) at redshift $z = 6.4\text{--}7.5$. The simulated galaxies show reasonable consistency with the observations across a wide range of stellar masses, except for the most extreme systems. Symbols are colored by the total infrared luminosity. The gray region shows the star-forming main-sequence relation at redshift $z = 6.7$ as measured by Speagle et al. (2014). Note that, for galaxy COS-87259, L_{IR} measurements exist for both an AGN component and thermal dust emission, where the latter value is plotted above.

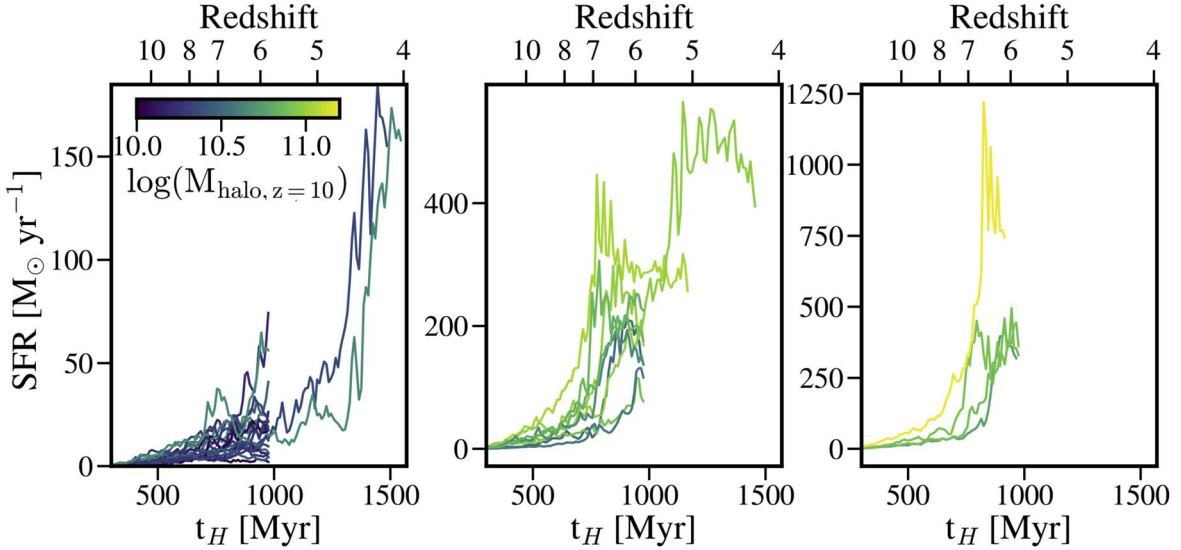


Figure 3. Cosmic Sands SFHs with galaxies binned according to their SFR at $z \sim 6$ and colored by their $z = 10$ halo gas masses. SFHs are diverse across halo mass, but the maximum SFRs are found in the highest-mass halos. The leftmost panel shows the relatively low-mass galaxies that have SFRs at $z = 6 < 80 M_{\odot}/\text{yr}$. Two galaxies in this bin that have evolved further show that the SFHs continue to rise. The middle panel shows galaxies with $80 < \text{SFRs} < 300 M_{\odot}/\text{yr}$ at $z = 6$, and the rightmost panel shows the four most star-forming galaxies at $z = 6$.

evolution over cosmic time of our sample to understand the context of their position on Figure 2. In Figure 3, we show the star formation histories (SFHs) for all galaxies, separated into bins according to their $z \sim 6$ SFR and color-coded by their initial ($z = 10$) parent halo gas masses. The galaxies in the leftmost panel have SFRs $< 80 M_{\odot} \text{yr}^{-1}$ at $z = 6$, and the galaxies in the rightmost panel have SFRs $> 300 M_{\odot} \text{yr}^{-1}$. SFRs scale with halo gas mass, and a majority of galaxy SFHs are rising over long timescales. While most of the simulations

are run to $z = 5.9$, some simulations have been evolved to lower redshift. We find that the galaxies in lower-mass halos that have evolved to $z \sim 4$ show steeply rising SFRs from $z = 4\text{--}5$ while higher-mass galaxies appear to hit a plateau near $z \sim 5$, similar to the trends seen in FLARES galaxies (Wilkins et al. 2022).

One major open question concerning early galaxy formation is whether or not massive early galaxies have significant star formation at times $z > 10$ or if their stellar population is

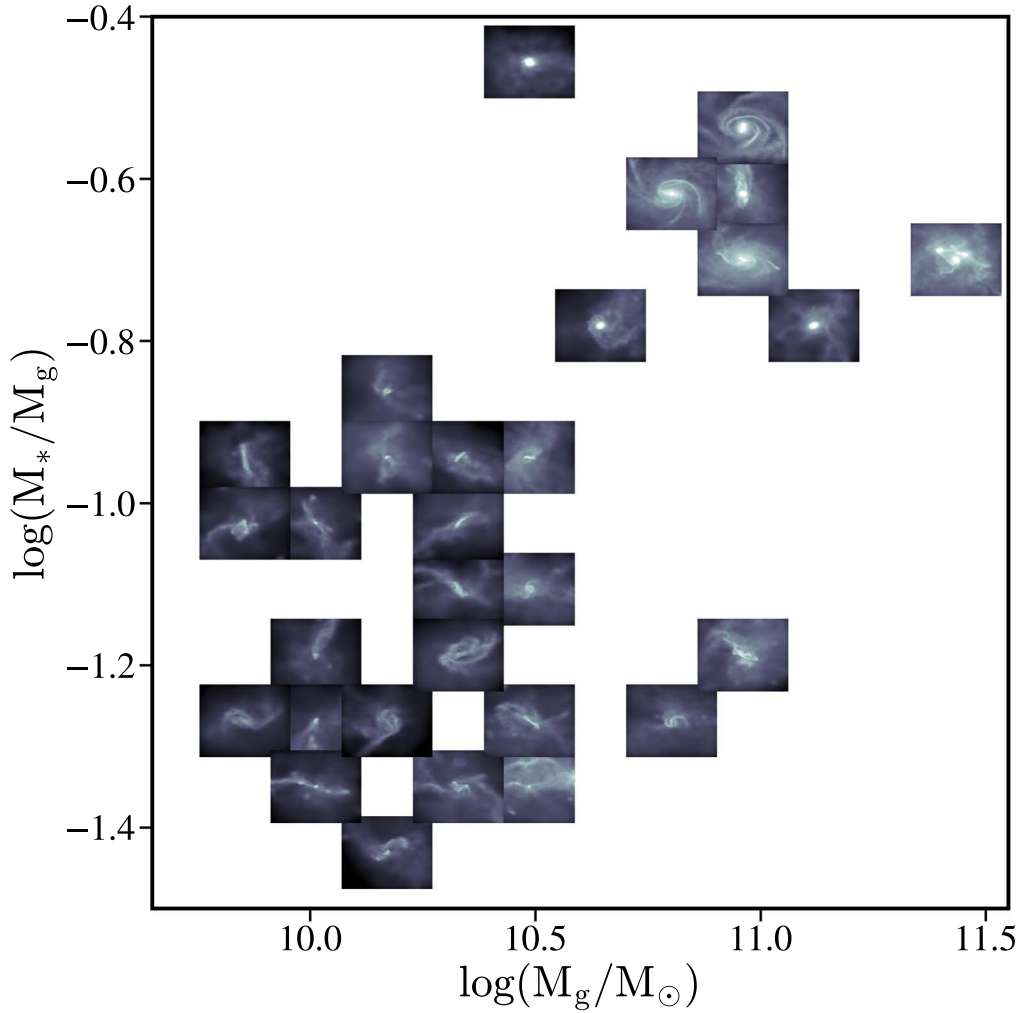


Figure 4. Early ($z = 6.7$) Cosmic Sands morphologies as a function of their gas mass and stellar-to-gas mass ratio. The galaxies are represented by projections of their gas surface density; each thumbnail spans 3 kpc with the observational angle chosen to align with the gas angular momentum vector. Galaxies with high gas masses have collapsed their gas into disks earlier, except for systems undergoing significant merger activity.

dominated by a single burst or sharply rising SFR near the time of observation. At $z = 6$, we find that galaxies with sharply rising SFHs have mass-weighted stellar ages that are dominated by their recent star formation, i.e., these galaxies are younger compared to their less star-forming counterparts. However, all galaxy SFHs appear to be monotonically (on timescales $\gtrsim 30$ Myr) rising; thus most of the galaxies' stellar populations are young (< 100 Myr) at these redshifts. However, due to the resolution dependence and uncertainties in star formation and feedback modeling, specific predictions about the onset of star formation are difficult to make robustly, as discussed in Section 5.2.2.

Morphologically, the galaxies are compact with a significant fraction of galaxies settling into rotationally supported disks by $z = 5$, with some systems forming a gas disk as early at $z = 7$. In Figure 4, we show the range of early Cosmic Sands morphologies as a function of stellar-to-gas mass ratio and total gas mass; each galaxy is represented by a 3 kpc thumbnail of the projected gas surface density at $z = 6.7$. The most gas-rich systems (and to a similar degree those with the largest stellar masses) tend to have more ordered rotation earlier, except for systems that are undergoing significant merger activity, although the exact cause of early disk formation and how this

correlates with galaxy growth is still somewhat uncertain (Hopkins et al. 2023). In Figure 5, we show one such example of a compact disk galaxy formed at $z = 6.9$. We plot the gas and stellar surface densities for two viewing angles (top row edge on, bottom row face on) and for two different times (left panel at $z = 6.9$, right panel at $z = 5.7$), showing the development of spiral arms over 200 Myr. In Appendix, we show a gallery of galaxies spanning the stellar mass range of the Cosmic Sands sample.

Star formation occurs primarily in the compact nuclear regions, resulting in the large stellar mass surface densities toward the center. We show the SFR surface densities in Figure 6, where we plot the SFRs as a function of galaxy total half-mass radius. The large SFR surface densities are comparable to observed values in high- z dusty, starburst systems (Ma et al. 2016; Aravena et al. 2016; Zavala et al. 2018, 2022).

Resulting from these SFRs, dust production primarily via SNe along with dust mass growth in the dense ISM enables large reservoirs of dust to exist by redshift 6.7. Hinted at in Figure 2, nearly a majority of the galaxies have infrared luminosities $\log(L_{\text{IR}}/L_{\odot}) > 12$, comparable to ultra-luminous infrared galaxies (ULIRGs) found at lower redshift. These large

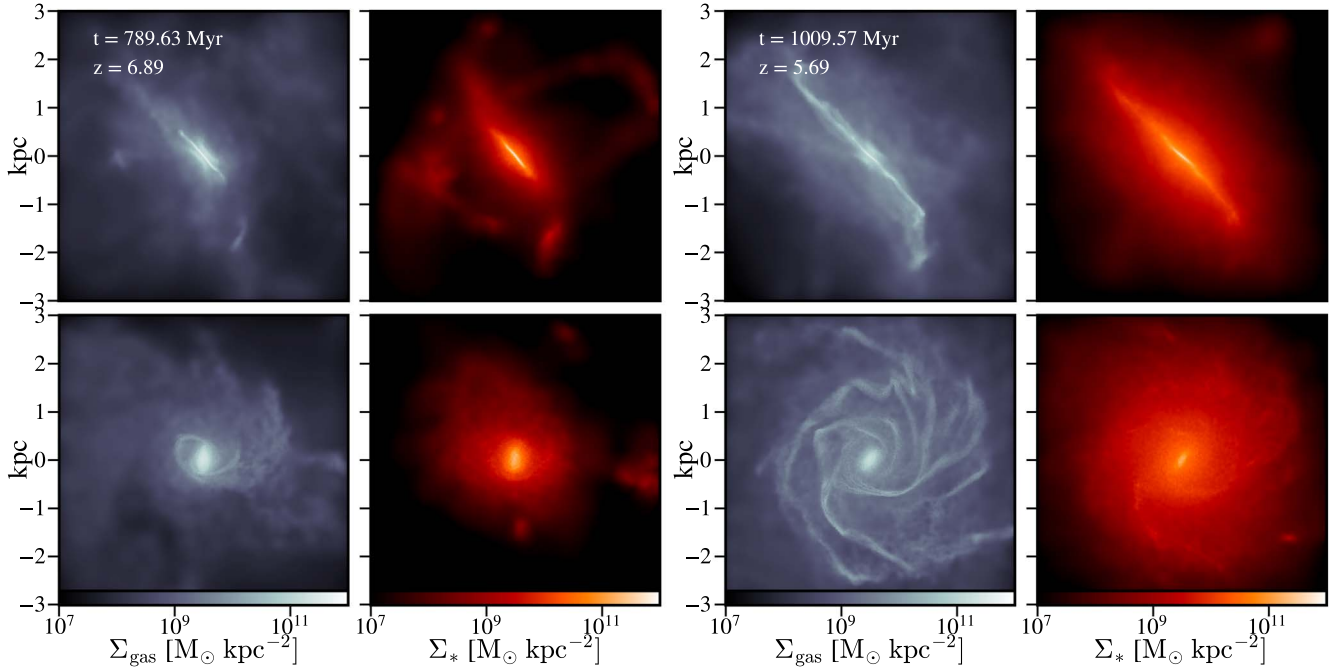


Figure 5. Example Cosmic Sands galaxy showing gaseous and stellar disk formation around $z = 7$. Disk formation proceeds relatively quickly in the more massive Cosmic Sands halos. The rows show the galaxy at two viewing angles (edge on vs. face on). The four panels on the left show the galaxy at $z = 6.9$, and the four right panels show the galaxy 200 Myr later at $z = 5.7$.

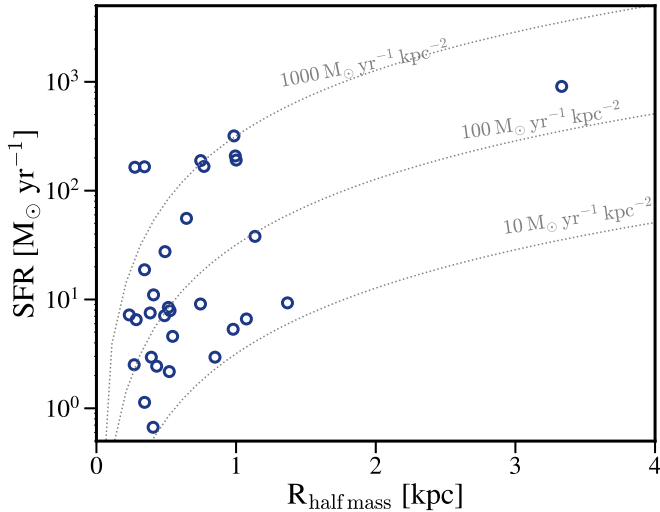


Figure 6. Star formation rate as a function of galaxy size for Cosmic Sands galaxies at $z = 6.7$. The size is defined as the total half-mass radius as measured by CAESAR, with the SFR equal to the instantaneous SFR within that radius. The gray dashed lines denote lines of constant SFR surface density. Most galaxies are compact with large SFR surface densities toward their nuclear regions.

infrared luminosities imply that large swaths of dust are heated by the young stars produced in galaxies with SFRs $\gtrsim 100 M_{\odot} \text{ yr}^{-1}$. In Figure 7, we show the dust masses as a function of stellar mass for the same galaxies in Figure 2. The Cosmic Sands galaxies exhibit a tight relation between their stellar and dust masses, with a dust-to-stellar mass ratio between 0.002 and 0.004, similar to the most massive systems in the original SIMBA 100 Mpc h^{-1} box. The galaxies from the literature span a larger range of dust-to-stellar mass ratios, ranging from 0.0007 to 0.05, although none are as dust rich as the most extreme systems, SPT0311-58 and COS-87259.

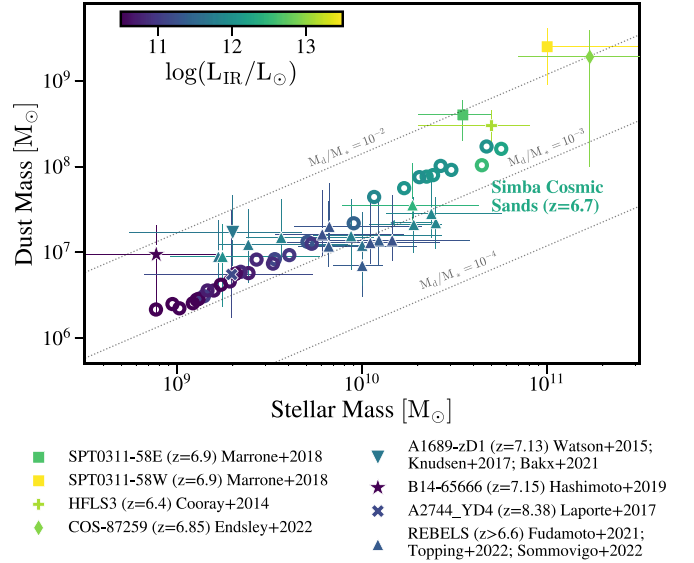


Figure 7. Dust mass as a function of stellar mass for the simulated galaxies and galaxies from the literature. Our Cosmic Sands galaxies span a dust-to-stellar mass ratio of 0.002 – 0.004, consistent with some REBELS sources and other normal dusty galaxies at this epoch. Symbols are colored by the total infrared luminosity. Dashed lines denote lines of constant dust-to-stellar mass ratios. Note that, for galaxy COS-87259, L_{IR} measurements exist for both an AGN component and thermal dust emission, where the latter value is plotted above.

3.3. Galaxy “Observable” Properties

We post-process our Cosmic Sands zoom-in simulations with 3D dust RT to infer the SEDs from the UV to the far-IR. This forward modeling allows us to represent our galaxies in the observable plane instead of the physical plane to allow for further comparisons to observations. In Figures 2 and 7, we have shown the infrared luminosities calculated from these mock SEDs, for one viewing angle. In Figure 8, we show the

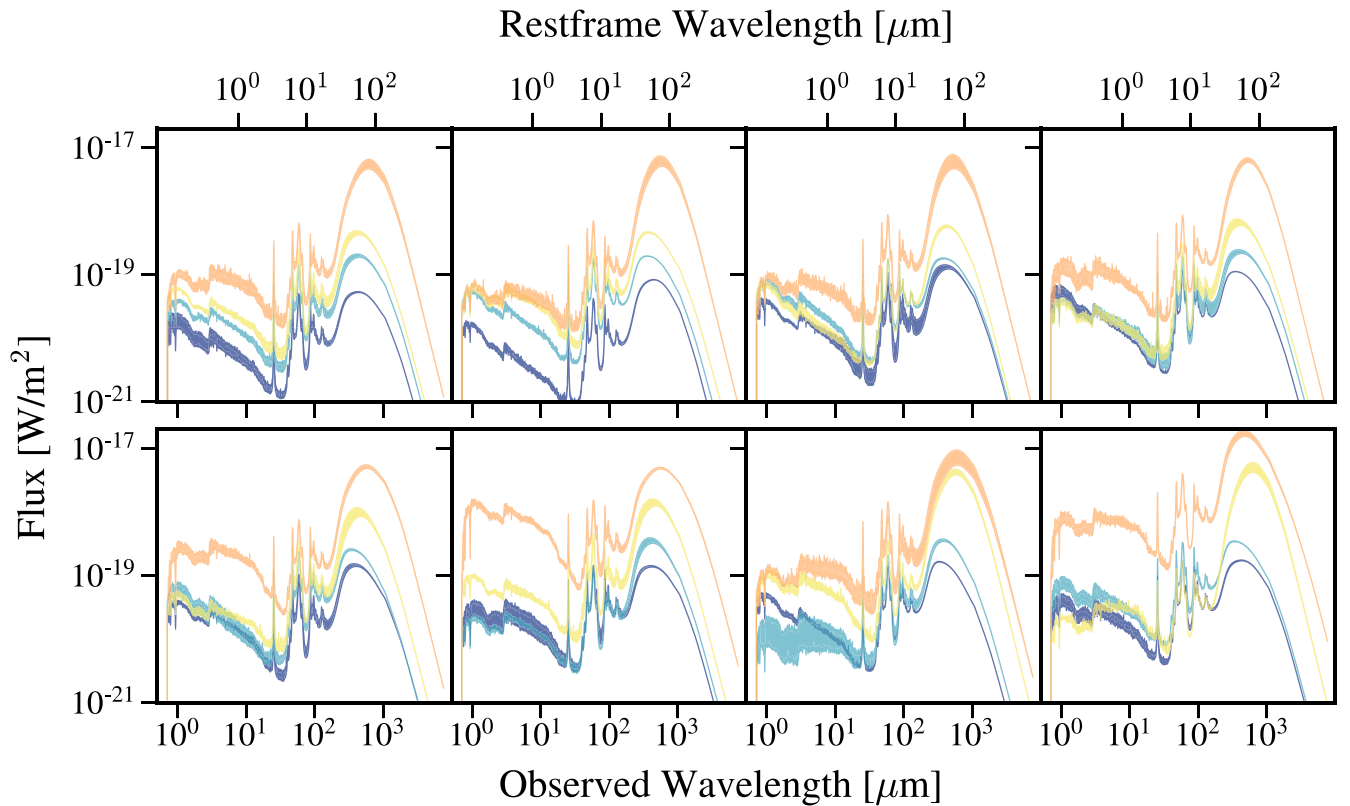


Figure 8. Spectral energy distributions (SEDs) for the central galaxies in each halo at redshift $z = 6.7$. The panels separate galaxies by total luminosity with binning chosen to achieve maximum clarity between each SED. In each panel, galaxies are represented by different colors. We create the SEDs at 25 different viewing angles, represented by the shaded regions for each galaxy. Some individual galaxies have a wide diversity in SED shapes as a function of viewing angle, thanks to inclination-angle-dependent dust attenuation.

galaxy SEDs binned by bolometric luminosity, such that galaxies are well separated in luminosity space for plot clarity. In each panel, the SED color denotes a galaxy, while the varying line thickness denotes SEDs generated from different viewing angles for each galaxy. For some galaxies, the SEDs are the same regardless of observer line of sight. For others, there is a spread of 0.1–0.2 dex in IR luminosity (with a proportional spread in UV luminosity) depending on viewing angle. This can be interpreted as an inclination-dependent SED: for galaxies exhibiting disk-like morphologies, the observed SED will vary significantly if viewed from an edge-on sightline, where a large fraction of stellar light is obscured by dust, versus the SED viewed from a face-on sightline, where the dust covering fraction is reduced. The morphology of a galaxy is in turn dependent on the stellar and dust growth history of the galaxy and parent halo, which we discuss in Section 4. Additionally, recent work by Lovell et al. (2021a) has shown similar results (that the orientation of a galaxy influences its observed SED), resulting in potential orientation-angle-driven selection biases.

In addition to SEDs, we have performed monochromatic imaging of a subsample of our Cosmic Sands galaxies in several bands. In Figure 9, we show a combined red giant branch (RGB) image of the most massive system in our sample at redshift $z = 6.62$, corresponding to rest-frame wavelengths of 0.4, 0.55, and 0.8 μm . This system undergoes a 2:1 merger event at $z = 6.45$ – 6.72 that triggers a starburst event. The leftmost image is the intrinsic image produced from the dust RT over a region of 50 kpc. The middle panel shows this image convolved with the Spitzer IRAC channels (1), (2), and (4)

point-spread functions (PSFs), filter transmission curves, and pixel scales ($1''.22 \text{ px}^{-1}$), although we do not model instrument noise and assume perfect signal-to-noise. With relatively low angular resolution, the multicomponent system is blended into an unresolved area of emission, from which determining the structure, kinematics, and physical properties of the galaxy would be challenging.

The rightmost panel of Figure 9 shows the intrinsic RGB image convolved with JWST NIRCcam (277w, 444w) and MIRI (770w) transmission curves, PSFs, and pixel scales ($0''.031^{-1}$ and $0''.1 \text{ pixel}^{-1}$, respectively). With an angular resolution nearly 2 orders of magnitude greater than the IRAC image, the mock JWST image resolves the multicomponent structure of the merger system.

4. What Drives Intense Star Formation and Infrared Luminosities in Early Massive Galaxies?

The Cosmic Sands simulation survey is intended to model massive galaxy evolution during the EoR. The physical properties of these modeled galaxies, as described in Section 3.2, include stellar masses, SFRs, and dust masses comparable to the most extreme systems ever detected at high redshifts. These populations of galaxies imply intense growth and metal enrichment over timescales of a few hundred million years. In this section, we aim to understand the origin of their intense properties. Specifically, we ask the following questions: What drives the extreme star formation in these massive systems? And do these SFRs power infrared luminosities comparable to observed galaxies?

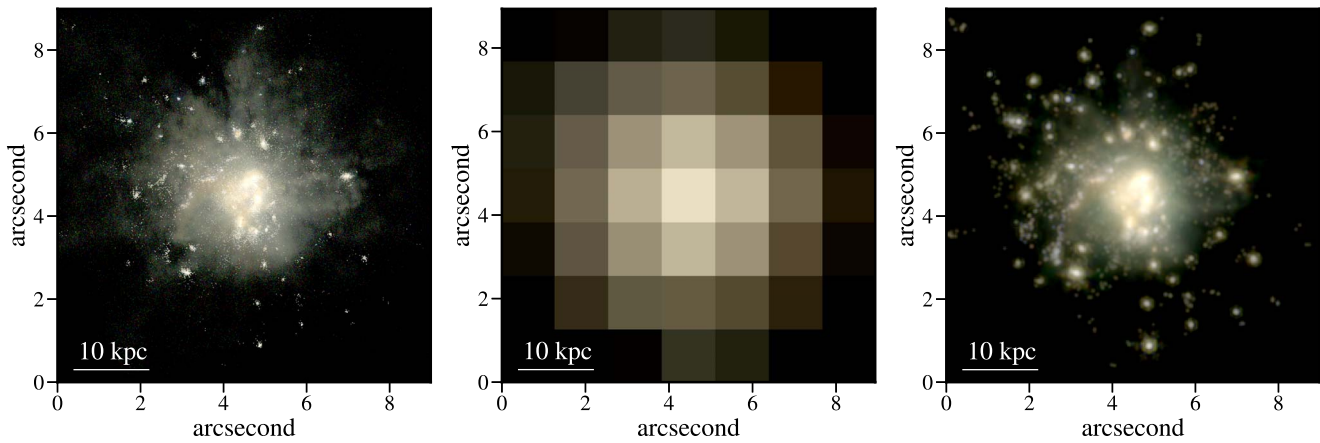


Figure 9. Mock RGB imaging of the merger-starburst system at redshift $z = 6.62$, approximately 10 Myr after in-fall of gas from the merger event. Left: intrinsic image of the galaxy. Middle: image convolved with Spitzer IRAC PSF and pixel scale. Right: image convolved with JWST NIRCам and MIRI PSF and pixel scales. The relatively poor angular resolution of the mock Spitzer observation blends together the structure of the merging system while the mock JWST observations resolve the individual galaxies.

4.1. Driving Early Star Formation

Sustaining large SFRs requires a significant supply of gas. In high-mass halos, two natural avenues for this gas accretion exist: filamentary accretion from the intergalactic medium (van de Voort et al. 2011; Sánchez Almeida et al. 2014), as well as major and minor galaxy mergers. In our simulations, we track the gas accretion rates on the central galaxies as a function of mode—accretion from filaments (and compact subhalo structure) versus accretion from major mergers. In practice, we define the contribution from major mergers by determining the bound progenitors of each galaxy over time and then computing the fraction of gas accreted from progenitors that are at least 50% of the central galaxy’s mass. Minor mergers are defined as the infall of CAESAR identified subhalo structure that is less than 50% of the central galaxy’s mass onto the central galaxy.

In Figure 10, we show the gas accretion history for a small subsample of our galaxies. We show for 4 galaxies the parent halo mass evolution (top row), the galaxy SFH (middle row), and the galaxy gas accretion history (bottom row). We have selected these four halos and their central galaxies to illustrate the gas accretion and SFR trends across the halo mass distribution. From left to right, the highlighted halos have gas masses at $z = 10$ of $2.24, 4.46, 9.49$ and $37.6 \times 10^{10} M_{\odot}$. In the top row of Figure 10, each panel shows all of the Cosmic Sands halos, with the chosen parent halos highlighted in bold. We show the evolution of halo gas masses from $z = 10$, to $z = 4 - 6$, with lines color-coded by the (instantaneous) maximum SFR achieved by each halo across its entire SFH. The halo gas mass distribution is the primary origin of the diversity of galaxy SFHs, shown in the middle row. The magnitude of SFRs increases from left to right, with the halo hosting the maximum starburst galaxy shown in the far-right column.

In each panel of the middle row, we plot the star formation histories of the central galaxies (blue lines) that occupy the halo highlighted in the top panel. We compare these SFHs to SFRs derived from the Speagle et al. (2014) main-sequence relation (black lines) as a function of time and current stellar mass, with the normalization equal to the cumulative stellar mass formed by the galaxy at that time. The star formation histories are calculated by binning the galaxy star particles by age and

inferring the initial mass of each particle with FSPS stellar population modeling, given the current population age, metallicity, and mass. Both low- and high-mass galaxies tend to track the main-sequence relation over time, with short (< 10 Myr) starburst periods that temporarily push the galaxy over the median main-sequence relation.

In the bottom row of Figure 10, we show the galaxy gas accretion rates for the four selected galaxies. We split the accretion into three categories, depending on the source: (1) inflow of gas parcels not bound to any subhalo structure (orange dots); (2) accretion of small, bound subhalos (light blue triangles); and (3) gas that is accreted onto the galaxy by way of major merger (maroon stars). The unbound gas accretion is the smooth gas accretion that tends to be steady with a rate set by the initial gas mass of the parent halo. Minor mergers are frequent for galaxies across the range of masses, but their relative contribution to the overall gas inflow rate is typically small. The gas accreted via major mergers (where we define *major* merger as an interaction between the central galaxy and a galaxy with at least 50% of the gas mass of the central) is not necessarily tied to the gas mass of the parent halo, meaning that major mergers occur in halos regardless of gas content. The impact of the major merger on the SFR of the central galaxy does appear to be a function of halo gas mass, as only galaxies in the most gas-rich halos undergo gas-rich major mergers with inflow rates comparable to the smooth accretion rates.

The impact of a major merger on a galaxy’s star formation is one that has been studied for many decades, and the link between starbursts and mergers has largely been established (Toomre & Toomre 1972; Sanders et al. 1988a, 1988b; Barnes & Hernquist 1991; Mihos & Hernquist 1994, 1996; Barnes & Hernquist 1996; Sanders & Mirabel 1996; Hopkins et al. 2008; Di Matteo et al. 2007; Cox et al. 2008). At high-redshift, however, the relative importance of star formation fueled via major merger is less clear (Kartaltepe et al. 2010; Kaviraj et al. 2013; Lofthouse et al. 2017; Duncan et al. 2019; Cibinel et al. 2019); in principle, in early gas-rich halos, large SFRs could be fueled entirely by smooth gas accretion alone (Finlator et al. 2006; Dekel et al. 2009). Indeed, the compact nature and abundance of gas in early massive halos and galaxies could mean the conditions for starburst activity are met without merger-induced torques driving gas inward. Furthermore, early major mergers may not have much impact on the proceeding

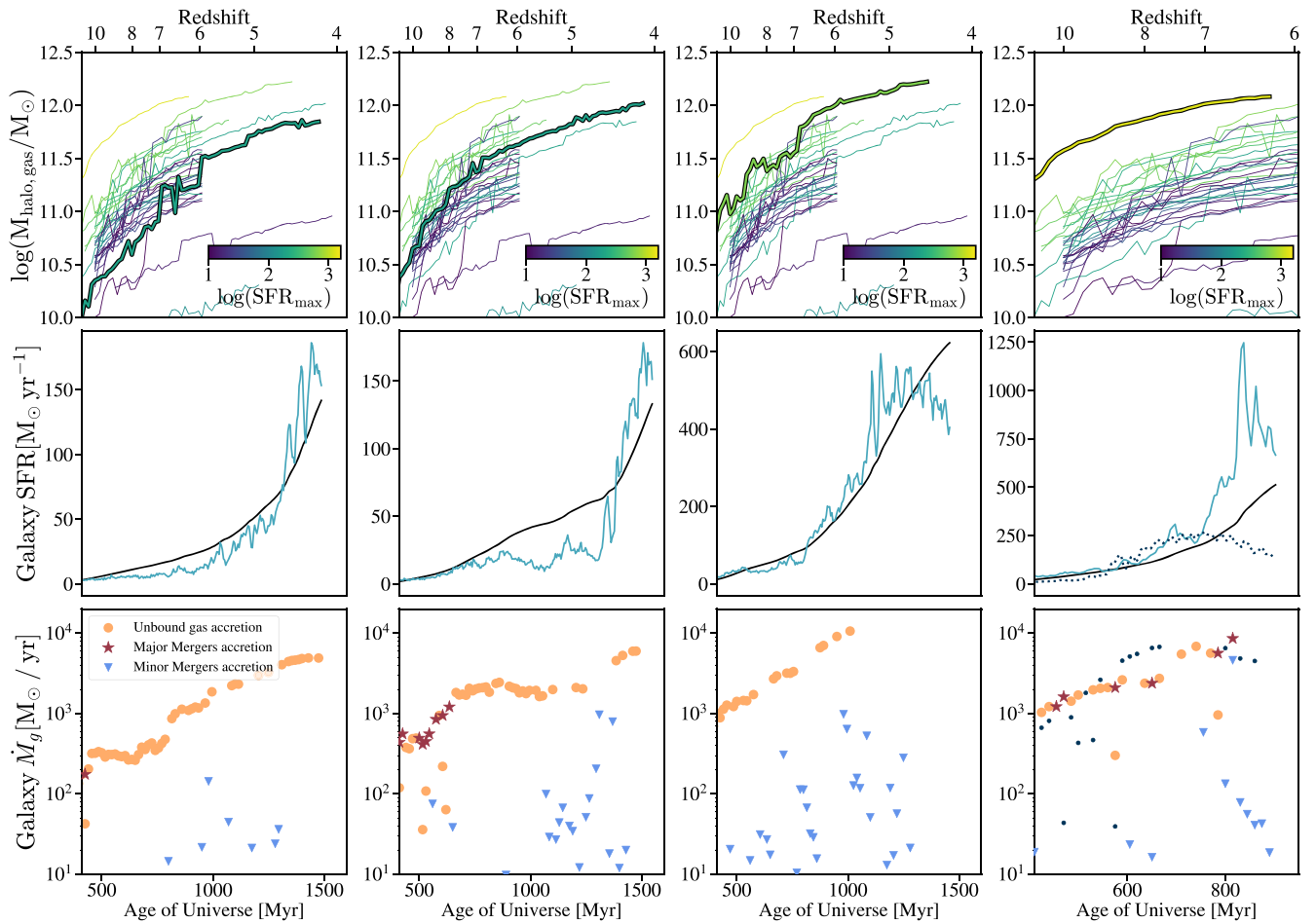


Figure 10. The growth history of selected Cosmic Sands galaxies. Top: halo gas masses as a function of time for all halos in the sample. The four columns highlight different halos that span the gas mass range, from lowest halo mass on the left to the most massive halo on the right. Middle: the star formation history of the central galaxy associated with the parent halo highlighted in the top panel of each column. The black line shows $\text{SFR}(t)$ compared to the main sequence in black, defined by the Speagle et al. (2014) slope and normalization set by the current stellar mass of the galaxy at each time. Bottom: gas accretion histories for the selected central galaxies. The orange dots show the accretion of smooth gas (e.g., unbound), the maroon stars show major mergers, where the gas mass ratio of the interacting galaxies is $>50\%$, and light blue triangles show the accretion from smaller minor mergers. The rightmost column shows the growth histories for the two nearly equal mass systems that occupy the halo. This is the only halo in our sample to host two such massive galaxies. The *nonmerger* system is shown by the dotted line in the middle panel and dark blue dots, showing the unbound gas accretion rate, in the bottom panel.

star formation due to inefficiencies in the gas torquing in galaxies that have not yet established rotationally supported disks (Barnes & Hernquist 1991; Fensch et al. 2016; Renaud et al. 2021).

In our sample of model galaxies that do not undergo interactions between gas-rich progenitors, the SFRs achieved by the nonmerger systems are substantially lower than their merger counterparts. The rightmost column of Figure 10 shows one such example of this: at redshifts ($z > 7$), the largest dark-matter halo in our sample hosts 3 roughly equal mass galaxies. The merger of two of these galaxies around 820 Myr sets off intense star formation, which boosts the merger system well above the star-forming main sequence for a period of 20 Myr. The merger progenitors were compact proto-disk galaxies, which provided ample torque to funnel the gas into a nuclear starburst. The growth history of the third galaxy within the same halo that did not experience a major merger is shown in the dashed lines; while the smooth gas accretion rates onto the comparably compact disk and the resulting star formation history were comparable to the merger system prior to 800 Myr, the galaxy-to-galaxy interaction made a significant difference between the two growth histories.

In contrast, the galaxy in the second column from the left experienced early major mergers that did not result in a significant elevation in star formation. There are several factors that can influence the impact a major merger has on the SFR of a galaxy. For one, the primary galaxy in the merger at $t_H \sim 500$ Myr was relatively low mass, with a gas mass of $\sim 2 \times 10^8 M_\odot$ and a stellar mass of $\sim 5 \times 10^7 M_\odot$. Second, the rate of gas accretion from the first of the series of mergers is $\sim 500 M_\odot \text{ yr}^{-1}$, which is nearly an order of magnitude smaller than the rate of accretion from the merger that did induce a starburst in the more massive halo. Lastly, upon examining the pre-merger and post-merger morphologies of this system, we find that the primary galaxy had not yet established an extended disk structure, which may have impacted the degree to which gas was able to funnel in to trigger a starburst (Barnes & Hernquist 1991). This is similar to the findings of Renaud et al. (2021), Segovia Otero et al. (2022), in which major mergers did not have significant impact on SFRs until a thick gas disk had formed in simulations of a Milky Way-like galaxy. The ISM of this system is highly dynamic, and so the additional turbulence of a major merger does not increase the efficiency of star formation. We conclude that the impact mergers have on early

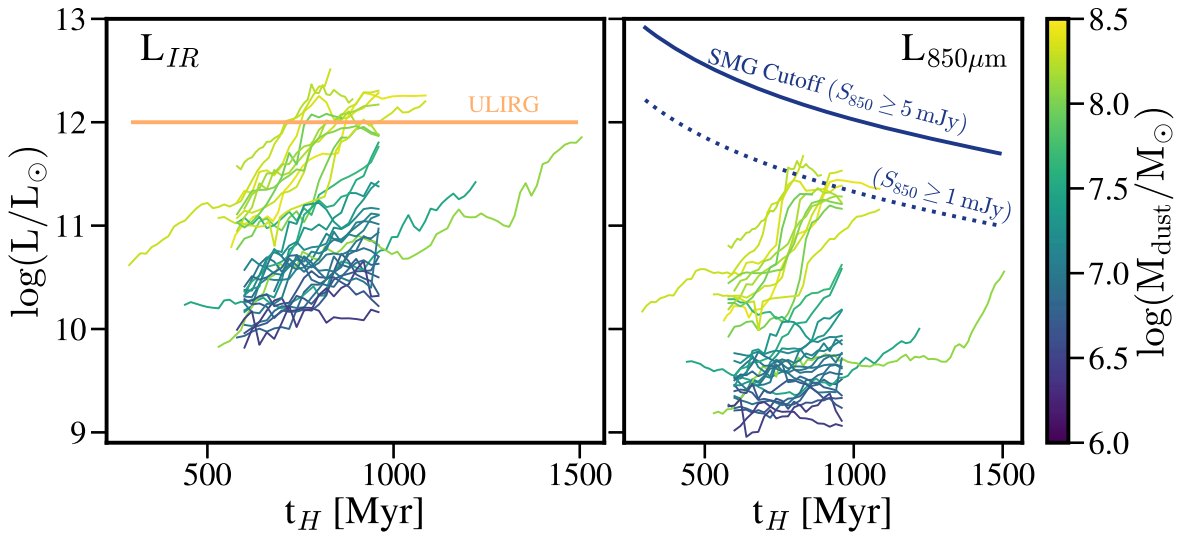


Figure 11. Luminosity evolution of the Cosmic Sands galaxies, showing that the most-dust-rich galaxies have ultra-luminous infrared galaxy (ULIRG)-like infrared luminosities over a prolonged period of time. Left: total infrared (8–1000 μm) luminosity as a function of time for the central galaxy in each halo. The lines are colored by the total galaxy dust mass at the latest snapshot. The orange line shows the ULIRG limit of $\log(L_{\text{IR}}) > 12$. Right: observed-frame 850 μm luminosity as a function of time. The solid (dotted) blue line denotes the flux density cutoff for a galaxy to be classified as an SMG: $S_{850} > 5 \text{ mJy}$ ($S_{850} > 1 \text{ mJy}$).

galaxy SFRs is dependent on several factors including the existence of a disk morphology to influence gas torquing. The formation of a disk morphology is itself also highly dependent on several factors including the halo accretion history (Sales et al. 2012). The most extreme SFRs in early galaxies appear to be the result of merger-induced starbursts, but note that, due to significant gas reservoirs, even secular SFRs are quite extreme with respect to the local universe, as demonstrated in Figure 2.

4.2. Infrared Luminosities and Chemical Enrichment

Although massive galaxies at low redshift are largely dispersion dominated elliptical systems that are seemingly devoid of star formation, the massive galaxy population of the early universe was extremely dynamic. These galaxies include compact starburst systems, mergers, dust-obscured AGN, and SMGs. Even by redshift $z = 6$, they are sufficiently chemically evolved to be observed in the rest-frame far-IR in dust emission. But to what degree are these phases common to all massive galaxies? In other words, how common is it, in our Cosmic Sands sample, for a galaxy to be observable as an FIR-bright SMG? The answer depends on several factors, including the star formation history of the galaxy, as explored above, and the timescale of thermal dust emission.

4.2.1. Defining an SMG

The various observational methods through which dust-obscured galaxies are identified result in several ways of defining exactly what an SMG is. The first submillimeter bright galaxies were detected from the ground within narrow atmospheric transmission windows around 850 μm and 850 mm. Those meeting a certain flux density cutoff (e.g., $S_{850\mu\text{m}} \geq 5 \text{ mJy}$) for sources targeted by the SCUBA instrument on JCMT (e.g., Smail et al. 1997; Barger et al. 1998; Hughes et al. 1998) were classified as SMGs (see review by Casey et al. 2014). Since then, the increased sensitivity of detectors on facilities like SPT and ALMA, as well as space-based telescopes targeting wavelengths inaccessible from the ground, have generally enabled classification of SMGs at

fainter observed fluxes and farther distances. Some major limitations of SMG detections are the large beam sizes and low angular resolution of far-IR instruments, which result in source confusing and blending. For instance, the beam size ($0.5 \times \text{FWHM}$) of the 250 μm band of Herschel SPIRE is $8''/8$, which corresponds to a spatial scale of approximately 76 kpc at $z = 2$, causing structures on smaller scales to become blended. With smaller beam sizes and higher resolution, SMGs can be deblended to reveal that the most extreme systems are comprised of smaller interacting galaxies and structures (Hodge et al. 2013; Karim et al. 2013; Hayward et al. 2013a, 2018). This is demonstrated in Section 3.3 with the mock rest-frame optical and FIR imaging as well as in recent ALMA observations of a high-redshift SMG presented in Spilker et al. (2022). In the context of comparisons between galaxy formation models and observations from the literature, consideration of the limitations of far-IR imaging is necessary to avoid biases in quantities like observed luminosity and sizes and to understand the impacts on galaxy SMG classifications (Hayward et al. 2011).

4.2.2. Are Cosmic Sands Galaxies SMGs?

Thermal emission from dust traces star formation over a longer timescale than other indicators (e.g., FUV luminosity and $\text{H}\alpha$ emission) and decreases at a slower rate compared to the drop off in star formation preceding a burst (Hayward et al. 2014; Ciesla et al. 2021; Flores Velázquez et al. 2021). Therefore, dust heated by a starburst could keep infrared luminosities boosted to SMG-like values for longer periods, depending on dust surface densities and star-dust geometries. Thanks to the chemical enrichment from evolved massive stars and dust growth in the ISM, we have shown in Figure 7 that the Cosmic Sands galaxies have dust masses comparable, within uncertainties, to both dust-obscured starburst systems, like SPT 0311-58E, as well as more normal $z = 6$ star-forming galaxies, like A1689-zD1.

We use POWDERDAY to generate the infrared luminosities, assuming Milky Way-like dust optical properties (see Section 2.3) for all available snapshots. In Figure 11, we show

the evolution of the infrared luminosities of the Cosmic Sands galaxies as a function of time. The most-dust-rich systems (9 out of 32 systems) achieve luminosities comparable to ULIRGs by $z = 8$ and maintain this IR brightness for over 500 Myr. The timescales over which the galaxies are infrared bright are therefore much longer than their SFH burst timescales, which are on the order of 10–100 Myr. IR bright phases are much less transient than starburst phases and appear to be a natural part of galaxy evolution for massive galaxies as suggested by Narayanan et al. (2015), Lovell et al. (2021b).

If we now consider the observed-frame 850 μm luminosity as a means to compare to classical SMG selection criteria, none of the Cosmic Sands galaxies are above the 5 mJy cutoff by $z = 5.8$. At $z = 6.7$, observed-frame 850 μm corresponds to a rest-frame wavelength of 110 μm , roughly straddling the contribution of warm and cold dust to the SED. Since none of the Cosmic Sands galaxies are above the 5 mJy cutoff, this could imply that the galaxies have warmer dust temperatures compared to classical SMGs (see Section 5.2.1). If we lower the selection criteria to 1 mJy, five of the most-dust-rich systems are above the threshold for >100 Myr.

Additionally, we find that there are no galaxies above this flux threshold at $z > 6$ in the SIMBA 100 Mpc h^{-1} volume, which matches the integrated SMG number counts and the number densities at $z = 2$ (Lovell et al. 2021b), suggesting that the Cosmic Sands simulation volume may be too small to form these extremely rare systems. Indeed, estimates for the number density of SMGs at $z > 6$ are $\sim 1 \times 10^{-7} \text{ Mpc}^{-3}$ (Reuter et al. 2020), which would imply 0.0125 sources with an infrared luminosity $> 3 \times 10^{12} L_{\odot}$ in the total Cosmic Sands volume. Thus while the volume-limited sample of Cosmic Sands galaxies does not have the extreme IR luminosities of classical SMGs, their physical properties (SFR, mass) are more comparable to the normal dusty galaxies at this epoch.

5. Discussion

The Cosmic Sands galaxies are illustrative representations of the evolutionary cycles of massive galaxies. Formed within gas-rich halos, these galaxies experience periods of concentrated gas accretion that fuels sustained star formation and starburst episodes, enabling the buildup of massive dust reservoirs and intense FIR emission. As presented in the previous section, while the formation history of these galaxies is diverse, a two-fold pathway emerges: smooth gas accretion can maintain SFRs above $250 M_{\odot} \text{ yr}^{-1}$, but to achieve SFRs that boost galaxies well above the main sequence, a larger perturbation, like a gas-rich major merger, is necessary to funnel enough gas into the galactic nucleus to trigger a starburst episode. And while the ULIRG-like infrared luminosities achieved by the most massive Cosmic Sands galaxies are impressive at such early times, none of the galaxies have bright enough FIR emission to be characterized as a classical SMG. In the following sections, we address follow-up questions that arise from our conclusions, including the fundamental uncertainties of our galaxy formation and stellar evolution modeling as well as comparisons to other models and a discussion on the future work we will do with the Cosmic Sands data set.

5.1. Comparisons to Other Models

Our understanding of early massive galaxy formation has progressed immensely during the last decade thanks to the advent of wide and deep observational surveys and the unprecedented sensitivity of facilities like ALMA and JWST. On the theoretical side, several modeling frameworks have made predictions for the earliest galaxy populations, focusing on the onset of star formation, chemical enrichment, and the contributors to the reionization of the universe. These predictions are now being tested with JWST probing the $z > 10$ redshift frontier, challenging the various modeling choices and uncertainties present in state-of-the-art simulations. Here, we compare our results to those from similar models, focusing on the analysis of hydrodynamical simulations of early galaxies.

The DUSTYGADGET simulations (Di Cesare et al. 2023) are a suite of eight statistically independent cosmological simulations, with a mass resolution of $5 \times 10^6 M_{\odot}$. Building on the work of Graziani et al. (2020), the authors use the DUSTYGADGET framework of galaxy formation to study the buildup of dusty normal galaxies at $z > 4$. The DUSTYGADGET galaxies span a wider range in stellar mass, owing to the larger effective simulation volume, but the high stellar mass galaxies have SFRs comparable to the Cosmic Sands galaxies, except for some Cosmic Sands galaxies that are elevated above the main-sequence relation. However, the high stellar mass DUSTYGADGET galaxies have larger dust masses when compared to Cosmic Sands galaxies of similar mass. The DUSTYGADGET dust-to-stellar mass ratios range between 0.006–0.01, an increase of about a factor of 3 from the Cosmic Sands galaxies.

The FirstLight simulations (Ceverino et al. 2017), with a comoving spatial resolution of ~ 100 pc, offer predictions for both low- and high-mass galaxies as cosmic dawn. They find that the SFHs of galaxies across a range of stellar masses are diverse, but most galaxies undergo several short ($\lesssim 100$ Myr) bursts of star formation early on in their formation, similar to the Cosmic Sands galaxies, as the similar time resolution of the snapshots can resolve short timescale SFR variations (Ceverino et al. 2018). Since the Cosmic Sands galaxies were chosen from the most massive halos, the galaxy property parameter space overlap between FirstLight and Cosmic Sands galaxies is limited, but the high-mass end of the FirstLight sample has comparable SFRs and gas depletion timescales to those from Cosmic Sands.

The FLARES simulations (Lovell et al. 2021c), with a baryonic mass resolution of $\sim 10^6 M_{\odot}$, model a range of overdensities in the EoR to explore the environmental dependence of early galaxy formation. The high-mass end of the FLARES stellar mass function ($M_{*} > 10^9$) has comparable SFRs to the Cosmic Sands galaxies, but due to our limited sample size, it is difficult to determine if the Cosmic Sands galaxies show the same high-mass star-forming main-sequence turnover. The analysis of SFHs in Wilkins et al. (2022) shows remarkable similarities between the FLARES and Cosmic Sands galaxies, namely that lower-mass galaxies have primarily rising SFHs toward $z = 5$ while higher-mass galaxies appear to hit a plateau.

Finally, VINTERGATAN is a high-resolution zoom-in simulation of a Milky Way-like galaxy (Agertz et al. 2021). While on the lower-mass end of the Cosmic Sands stellar mass range, at $z > 4$, the Milky Way progenitor has a rising SFR and experiences a continuous stream of gas accretion from

bombardment of small subhalos and gas streamers. The galaxy’s thick disk does not form until $z \sim 2.7$, and so major mergers do not impact the SFR significantly (Renaud et al. 2021; Segovia Otero et al. 2022). Similarly, the higher-mass Cosmic Sands galaxies tend to form disks sooner while the lower-mass galaxies remain unorganized and are less impacted by mergers.

5.2. Modeling Uncertainties

5.2.1. Dust Properties and Infrared Luminosities

The success of the Cosmic Sands simulations to reproduce the population of extreme massive systems in the early universe is primarily due to the galaxy formation physics within SIMBA as well as the ability to self-consistently model dust growth and star-dust geometries. As shown in Section 3.2, our galaxies have comparable stellar and dust masses and SFRs to some of the systems observed at similar epochs. However, the radiative properties of the galaxies, specifically the infrared luminosities, are in mild tension with the observations. For example, at a fixed stellar mass, the infrared luminosities from the simulated galaxies occupy a narrower range than those observed. We show this explicitly in Figure 12, where we plot the light-to-mass ratios for both stellar and dust mass as a function of stellar mass. The Cosmic Sands galaxies (dark blue in the top two panels) occupy a narrow range in light-to-mass ratio over the range of galaxy stellar mass.

Although the differences are slight, the implications of the lack of overlap in parameter space are potentially significant. For instance, several uncertainties in the forward modeling of the Cosmic Sands galaxies exist, including the stellar population modeling (the IMF, stellar isochrones, and the stellar spectral library chosen to model the luminosity of the star particles; see, e.g., Akins et al. 2022), the handling of unresolved emission from H II and photodissociation regions in the birth-clouds surrounding young stars, and the assumed optical properties of the dust grains and thus the underlying extinction curve of the galaxy spectrum. Modifying the optical properties of the dust grains would propagate changes in the resulting infrared luminosity for the same dust and stellar mass values. For a galaxy with fixed dust mass, if the dust attenuation law is made steeper, while keeping the V-band optical depth fixed, the amount of UV stellar light reprocessed by dust would increase, which would lead to an increase in IR luminosity per mass of dust. Constraints on the optical properties of dust at high redshift are not widely available; thus, we elect to use a fixed dust extinction curve that matches the average Milky Way curve. However, recent numerical studies including an evolving dust grain size distribution in Li et al. (2020; see also Makiya & Hirashita 2022) have shown that galaxies can initially exhibit steep dust extinction curves that then evolve toward shallower UV–optical slopes as the grain size distribution evolves to match the Mathis, Rumpf & Nordsieck (MRN) distribution (Mathis et al. 1977).

At the same time, there may be significant uncertainties in the observed infrared luminosities and dust masses of high- z galaxies. For example, if the FIR SED is not fully sampled—a scenario that is common—then the derived dust properties are highly degenerate and dependent on modeling choices. One common solution is to assume a fixed dust temperature and optically thin modified blackbody emission to derive the dust mass (e.g., Laporte et al. 2017; Fudamoto et al. 2021;

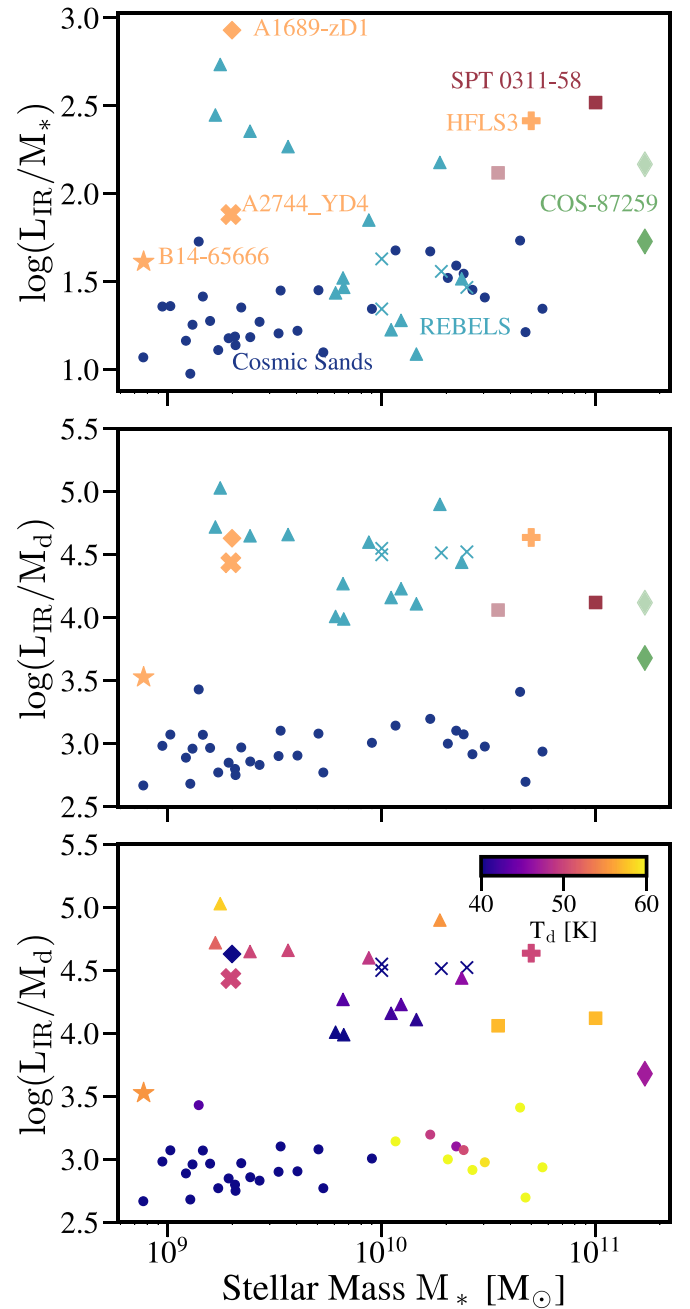


Figure 12. Ratio of galaxy infrared luminosity to stellar mass (top) and dust mass (middle), with the bottom panel showing the IR luminosity-to-dust mass ratio with points colored by derived or assumed dust temperature. In the top two panels, the Cosmic Sands galaxies are shown in dark blue points, while the other points are the observations’ comparison sample from Figures 2 and 7. The Cosmic Sands galaxies occupy a narrower range of luminosity-to-mass ratios compared to the observations at fixed stellar mass. The western (eastern) source of SPT 0311-58 is shown in dark (light) red. COS-87259 (Endsley et al. 2022) has contributions to the IR luminosity from both dust (darker green point) and an obscured AGN (lighter green). Dust temperatures for REBELS galaxies (thin X’s, Fudamoto et al. 2021), COS-87259 (long diamond, Endsley et al. 2022), and A2744_YD4 (thick X, Laporte et al. 2017) are assumed in order to derive dust masses and IR luminosities. HFLS3 (plus, Cooray et al. 2014) is fit with a two temperature dust model and find that 90% of the dust mass is in the warm component (50 K), which we plot here.

Endsley et al. 2022). From the POWDERDAY RT, we derive mass-weighted dust temperatures for the Cosmic Sands galaxies at $z = 6.7$ and find a median temperature of 45 K with a range of 30–80 K, as shown in the bottom panel of

Figure 12. The temperatures corresponding to the peak of FIR emission, a proxy for luminosity-weighted dust temperature, range from 40–70 K, with variations up to 10 K for individual galaxies depending on the viewing angle of the SED. If we assume a dust temperature of 45 K for all Cosmic Sands galaxies and assume modified blackbody emission, the inferred dust masses can differ by up to a factor of 5.

Furthermore, although SIMBA has been shown to match the dust properties of $z=0-2$ galaxies (Li et al. 2019; Dudzevičiūtė et al. 2021), uncertainties remain with regards to modeling the buildup of dust in the early universe, including the processes of dust production from stellar sources and dust growth in the ISM. While systematically testing various dust models is beyond the scope of this work, in a future study, we will focus on analyzing these uncertainties and degeneracies in dust modeling with a particular focus on the efficiency of dust growth in the EoR.

Lastly, we note that we do not model any AGN emission for the Cosmic Sands galaxies. This is motivated by several factors including uncertainties in BH seeding at the earliest epochs and in the adopted AGN spectra for use in radiate transfer. Thus, the measured infrared luminosities are a result of reprocessed starlight alone. Recently, however, Endsley et al. (2022) reported luminosity estimates for COS-87259 with contributions from AGN and starlight-heated dust. These two values are shown in Figure 12. The starlight-heated dust measurement (dark green) is more in agreement with the light-to-mass ratios of the Cosmic Sands galaxies. This could imply that some of the discrepancies in our luminosity values originate from neglecting AGN emission, in addition to the heating of diffuse dust by the AGN source. If we calculate the AGN luminosities corresponding to the BHs that have formed in 4 systems from $z=4-6.7$, we find that AGN luminosities are anywhere from 3% to 45% of the galaxies’ (AGN free) bolometric luminosities. Though, how this AGN luminosity contributes to the heating of diffuse, nontorus dust remains uncertain (see, e.g., McKinney et al. 2021). We conclude that AGN emission may matter in terms of dust heating at high redshift, but is ultimately outside the scope of this work and is left to future analysis.

5.2.2. Stellar Feedback

While the SIMBA suite of galaxy formation physics allows us to self-consistently model complex galaxy growth histories and dust mass build up in massive halos, as a necessity, processes like star formation and the internal physics of molecular clouds are not explicitly modeled due to resolution constraints. For instance, star formation and the structure of the ISM are modeled with an effective equation of state that is tuned to reproduce the Kennicutt (1989)–Schmidt (1959) relation. The star formation histories that result from an effective equation of state have been shown to be steadier and less prone to burstiness compared to models, like FIRE (Hopkins et al. 2014) and SMUGGLE (Marinacci et al. 2019). Sparre & Springel (2016) showed that the resolution of a simulation also plays a role in the burstiness of galaxy SFHs, with strong bursts present only in simulations with the highest resolution ($m_{\text{gas}} \sim 1-2 \times 10^5 M_{\odot}$).

As shown in Hopkins et al. (2014), the explicit modeling of stellar feedback processes results in SFHs that are quantitatively different than the SFHs produced by models employing subgrid resolution prescriptions, owing primarily to the coupling of the various feedback processes that is not

reproducible by only characterizing the net effects of feedback. Namely, the SFHs produced by the FIRE model peak in star formation later and have greater short timescale variability compared to models without explicit feedback models (Iyer et al. 2020).

This represents a fundamental uncertainty in modeling massive galaxy formation and evolution; the “burstiness” of real galaxy star formation histories is itself an uncertain quantity due to the challenges of inferring small timescale variations in the SFH and even large starburst episodes from SED modeling (e.g., Iyer et al. 2019).

6. Summary and Conclusions

In this paper, we present the Cosmic Sands sample of massive galaxies in the EoR. Built on the SIMBA model for galaxy formation, we produce 32 dark-matter halos with gas-rich central galaxies featuring SFRs as high as $1000 M_{\odot} \text{ yr}^{-1}$. We show that the Cosmic Sands galaxies span a wide range of stellar masses and SFRs, matching some of the “normal” star-forming dusty galaxy population of, e.g., REBELS (Bouwens et al. 2022; Topping et al. 2022) as well as the extreme starburst and SMG systems of HFLS3 (Riechers et al. 2013) and SPT 0311-58E (Marrone et al. 2018). Below we summarize the notable findings of our analysis:

1. At redshift $z=10$, proto-massive galaxies are extremely compact and undergo nearly continuous bombardment of gas accretion from both smooth gas streams and mergers with other subhalos. But by $z=6$, some systems have evolved into disk-like galaxies with distinct gas dense spiral arms and compact star formation in their nuclei.
2. Smooth gas accretion can maintain SFRs above $250 M_{\odot} \text{ yr}^{-1}$, but to achieve SFRs that boost galaxies well above the main sequence, a larger perturbation like a gas-rich major merger is necessary to trigger a starburst episode. Thus, we conclude from Section 4 and Figure 10, that, while rare, dusty starburst galaxies in the early universe are primarily merger driven.
3. Coupling the Cosmic Sands simulations with dust RT, we find that the infrared luminosities at $z \sim 6$ of the most-dust-rich systems are comparable to local ULIRGs but are substantially dimmer than the extreme SMG systems. Since the physical properties of the galaxies are comparable to the observed sample of galaxies, except for the extreme systems of SPT0311-58W and COS-87529, we suggest that this discrepancy could be due to modeling uncertainties (dust optical properties, stellar feedback models) and difficulties in measuring dust properties of observed galaxies, as discussed in Section 5.2.1.

The galaxies in the Cosmic Sands sample are an ideal laboratory to study in detail the processes that influence massive galaxy formation and evolution. While not wholly representative of all early massive galaxies, they are rather illustrative examples highlighting the various pathways galaxies take during their evolution, from major merger events to starbursts and SMG phases. The primary question we aim to address with Cosmic Sands is under what conditions do massive, dusty, and extreme systems form, and what is their subsequent fate?

One major question concerning early massive, dusty galaxies is how do they achieve such large dust-to-stellar mass ratios? Studies into the predicted dust yields from Type II SNe and

winds from evolved stars reveal that the theoretical estimates are in tension with observed dust masses in galaxies at $z > 6$ (Michałowski 2015; Mancini et al. 2015; Ginolfi et al. 2018; Leśniewska & Michałowski 2019; Graziani et al. 2020; Di Cesare et al. 2023). The lack of constraints on basic dust properties such as composition and grain size distribution, due to the uncertainties about the ISM conditions that drive the growth and destruction of dust grains, makes modeling the buildup of dust challenging (Burgarella et al. 2020).

While the SIMBA galaxy formation framework has been shown to reproduce dust properties at redshifts $z = 0 - 2$, what remains unclear is the contribution of the various dust formation pathways to the overall dust content in a galaxy, especially at higher redshifts. We aim to address these uncertainties in future studies by comparing various methods for dust implementations in cosmological simulations.

Acknowledgments

The authors would like to thank Sune Toft, John Weaver, and Gergo Popping for fruitful discussions that guided the analysis of this paper, and Dan Stark and Michael Topping for sharing their stellar mass measurements for the REBELs sources. The Cosmic Dawn Center is funded by the Danish National Research Foundation under grant No. 140. S.L. and D.N. acknowledge support from the NSF via grant AST-1909153. This work was initiated at the Aspen Center for Physics, which is supported by NSF grant PHY-1607611.

The SIMBA simulations used in this work were run on the Hipergator computing cluster at the University of Florida. The flagship SIMBA simulations were run on the ARCHER U.K. #National Supercomputing Service <http://www.archer.ac.uk>.

Software: SIMBA (Davé et al. 2019), MUSIC (Hahn & Abel 2011), CAESAR (Thompson 2014), POWDERDAY (Narayanan et al. 2021), HYPERION (Robitaille 2011), NUMPY (van der Walt et al. 2011), MATPLOTLIB (Caswell et al. 2018), PANDAS (McKinney 2010; pandas development team 2020), ASTROPY (Virtanen et al. 2020), YT (Turk et al. 2011), SPHVIEWER (Benitez-Llambay 2015).

Appendix Morphologies of $z \sim 6$ Galaxies

Here we present gas- and stellar-mass surface densities at edge-on and face-on observing angles for a subsample of Cosmic Sands galaxies to compliment the galaxy shown in Figure 5. In Figures 13–18, the four left-hand panels show the surface densities at an early epoch, and the right-hand panels show the densities at a later epoch for the same galaxy. Observing angles are chosen based on the angular momentum vector of the gas in the galaxy as a proxy for the normal vector, although, in some systems without ordered rotation, the normal vector is not well defined, and *edge-on* and *face-on* views are chosen by eye.

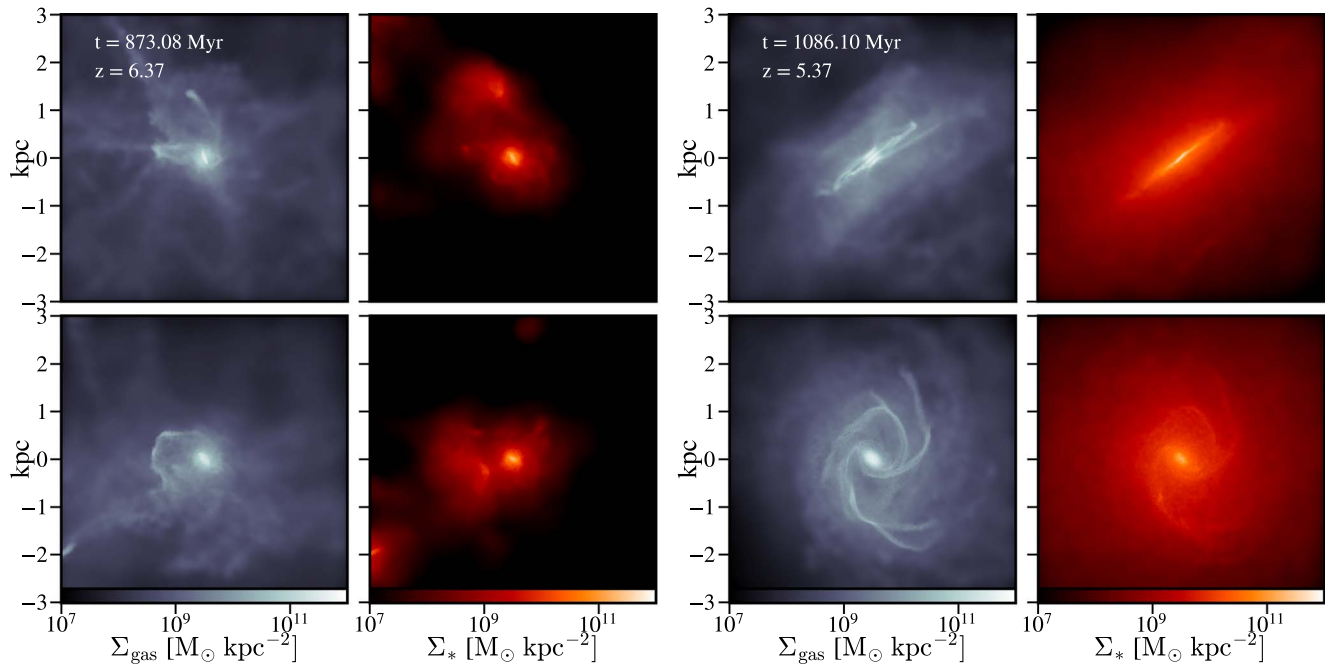


Figure 13. Same as Figure 5 but for a different galaxy. The rows show the galaxy at two viewing angles (edge on vs. face on). The four panels on the left show the galaxy at $z \sim 6.4$, and the four right panels show the galaxy 200 Myr later at $z \sim 5.4$.

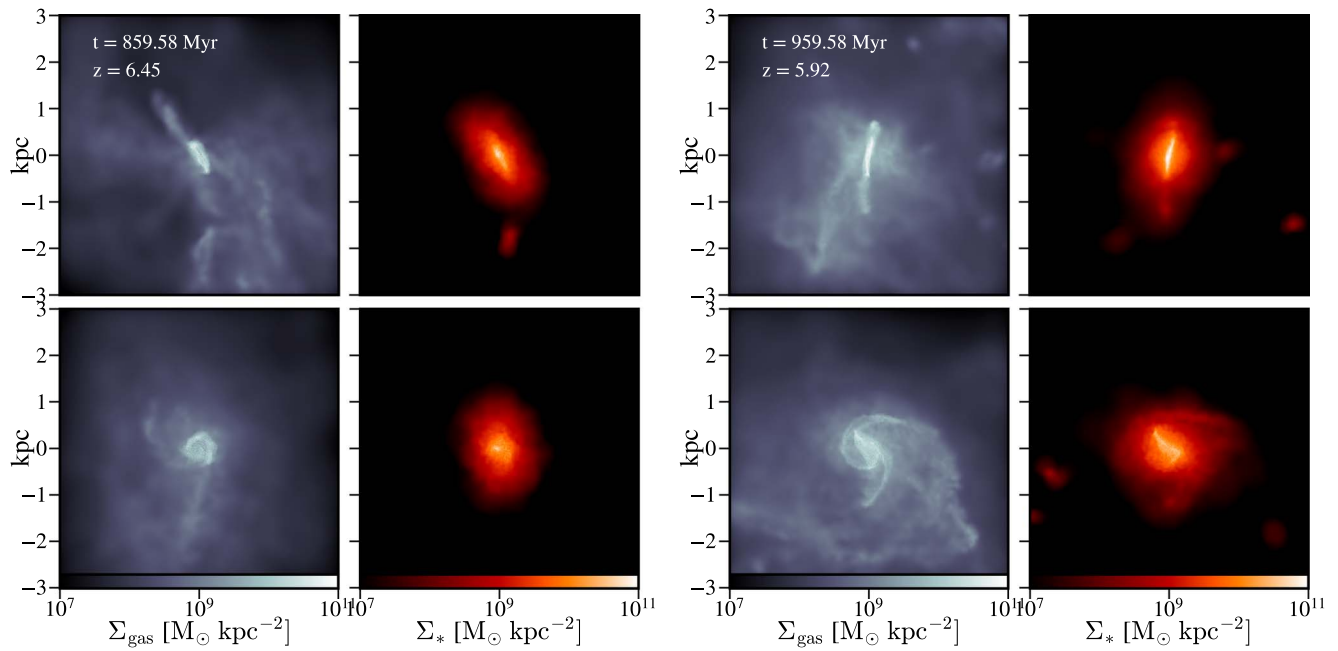


Figure 14. Same as Figure 13 but for a different galaxy.

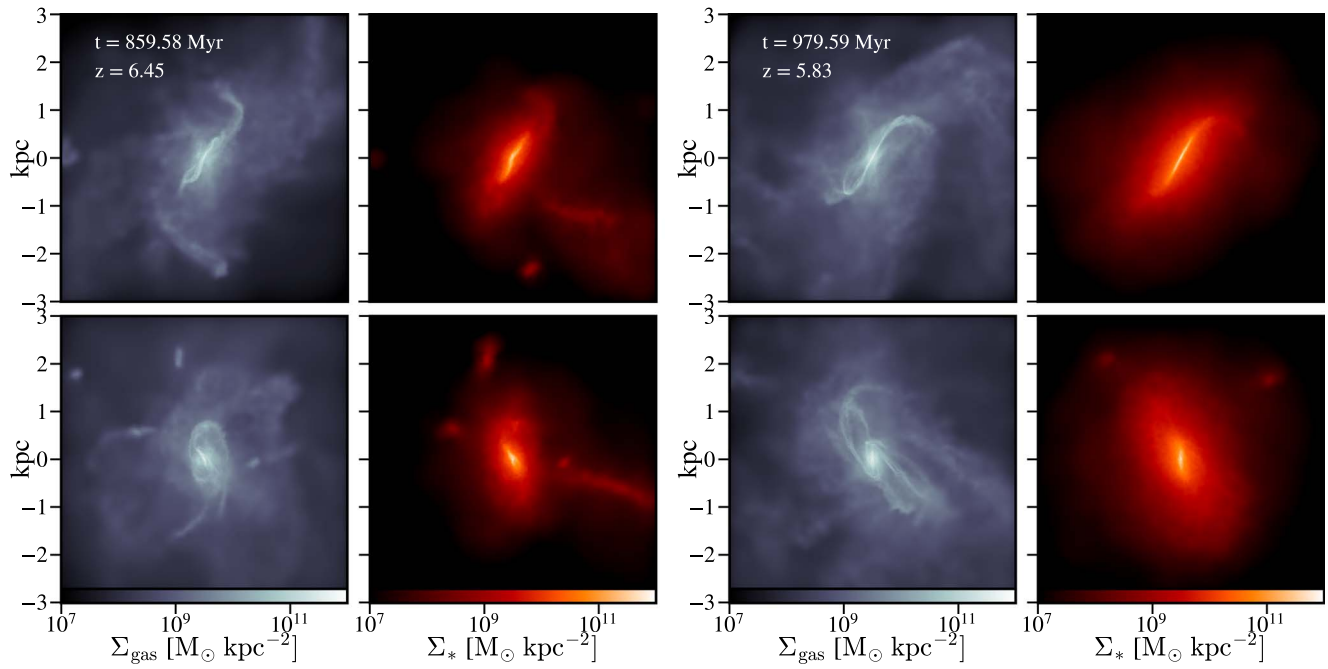


Figure 15. Same as Figure 13 but for a different galaxy.

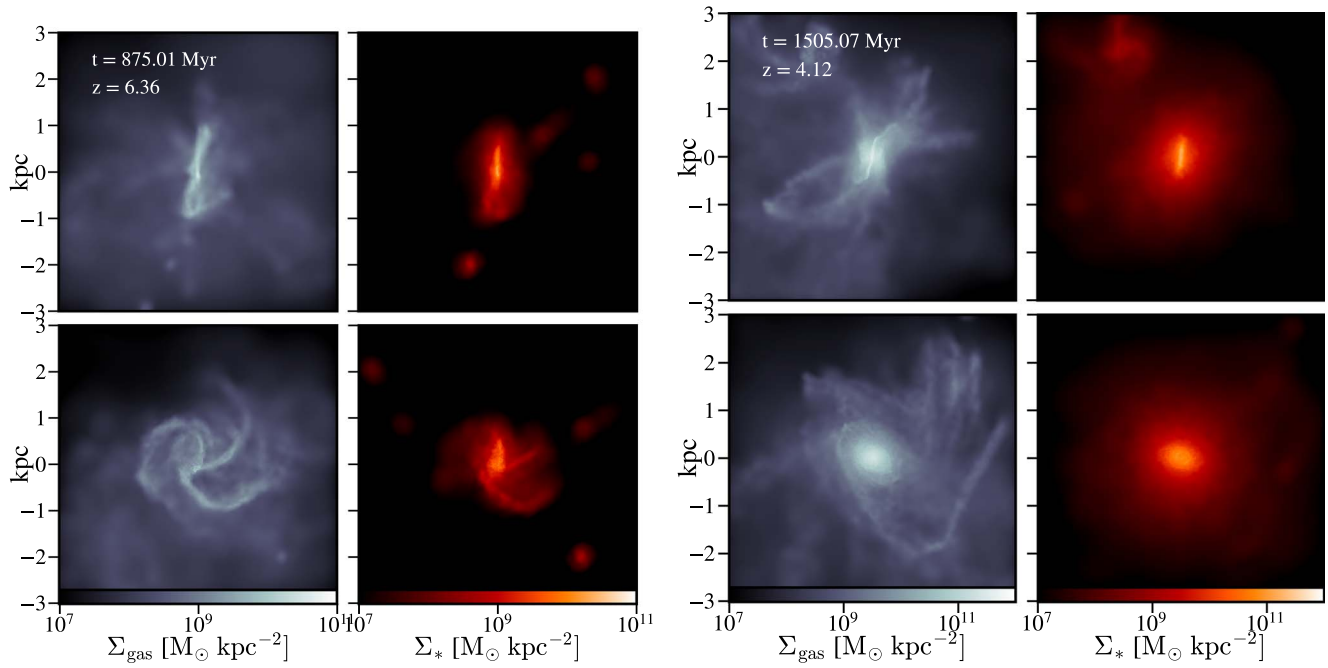


Figure 16. Same as Figure 13 but for a different galaxy.

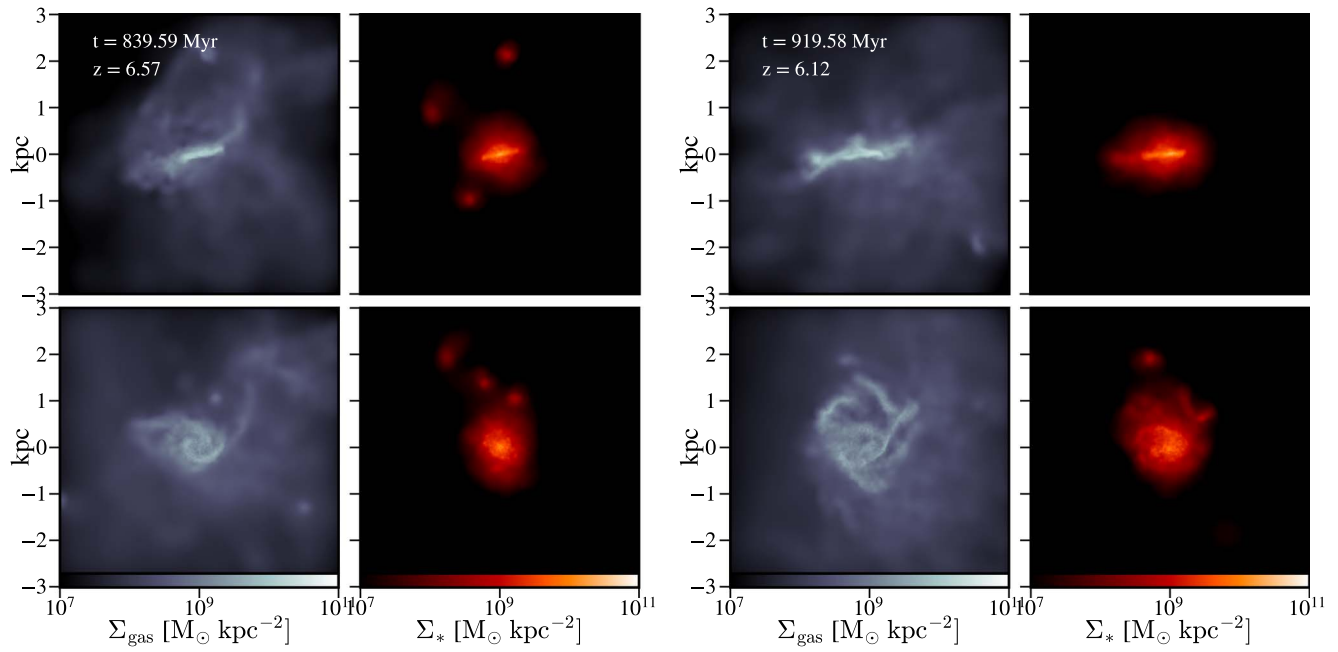


Figure 17. Same as Figure 13 but for a different galaxy.

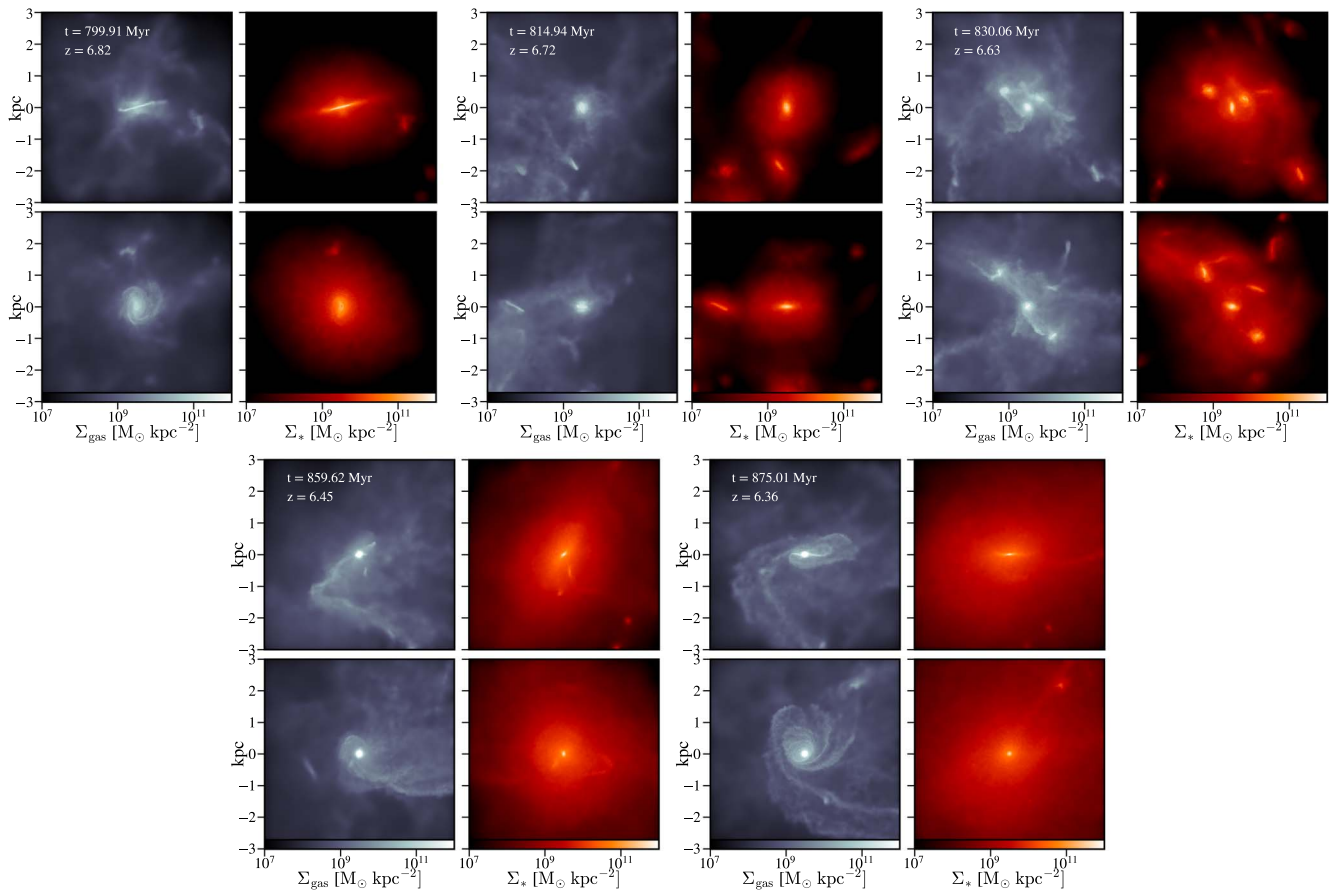






Figure 18. The maximum starburst example undergoing a major merger over 80 Myr.

ORCID iDs

Sidney Lower  <https://orcid.org/0000-0003-4422-8595>
 Desika Narayanan  <https://orcid.org/0000-0002-7064-4309>
 Qi Li  <https://orcid.org/0000-0001-8015-2298>
 Romeel Davé  <https://orcid.org/0000-0003-2842-9434>

References

- Agertz, O., Renaud, F., Feltzing, S., et al. 2021, *MNRAS*, 503, 5826
 Akins, H. B., Narayanan, D., Whitaker, K. E., et al. 2022, *ApJ*, 929, 94
 Anglés-Alcázar, D., Faucher-Giguère, C.-A., Quataert, E., et al. 2017, *MNRAS*, 472, L109
 Aoyama, S., Hirashita, H., & Nagamine, K. 2020, *MNRAS*, 491, 3844
 Aoyama, S., Hou, K.-C., Hirashita, H., Nagamine, K., & Shimizu, I. 2018, *MNRAS*, 478, 4905
 Aravena, M., Spilker, J. S., Bethermin, M., et al. 2016, *MNRAS*, 457, 4406
 Bakh, T. J. L. C., Sommovigo, L., Carniani, S., et al. 2021, *MNRAS*, 508, L58
 Barger, A. J., Cowie, L. L., Sanders, D. B., et al. 1998, *Natur*, 394, 248
 Barnes, J. E., & Hernquist, L. 1996, *ApJ*, 471, 115
 Barnes, J. E., & Hernquist, L. E. 1991, *ApJL*, 370, L65
 Baugh, C. M., Lacey, C. G., Frenk, C. S., et al. 2005, *MNRAS*, 356, 1191
 Behroozi, P., Wechsler, R. H., Hearin, A. P., & Conroy, C. 2019, *MNRAS*, 488, 3143
 Benitez-Llambay, A. 2015, py-sphviewer: Py-SPHViewer v1.0.0, Zenodo, doi:10.5281/zenodo.21703
 Béthermin, M., Wu, H.-Y., Lagache, G., et al. 2017, *A&A*, 607, A89
 Bianchi, S., & Schneider, R. 2007, *MNRAS*, 378, 973
 Bouwens, R. J., Smit, R., Schouws, S., et al. 2022, *ApJ*, 931, 160
 Burgarella, D., Nanni, A., Hirashita, H., et al. 2020, *A&A*, 637, A32
 Casey, C. M., Narayanan, D., & Cooray, A. 2014, *PhR*, 541, 45
 Caswell, T. A., Droettboom, M., Hunter, J., et al. 2018, Matplotlib/Matplotlib V3.0.1, Zenodo, doi:10.5281/zenodo.1482098
 Ceverino, D., Glover, S. C. O., & Klessen, R. S. 2017, *MNRAS*, 470, 2791
 Ceverino, D., Klessen, R. S., & Glover, S. C. O. 2018, *MNRAS*, 480, 4842
 Chapman, S. C., Blaín, A., Ibata, R., et al. 2009, *ApJ*, 691, 560
 Choban, C. R., Keres, D., Hopkins, P. F., et al. 2022, *MNRAS*, 514, 4506
 Choi, J., Dotter, A., Conroy, C., et al. 2016, *ApJ*, 823, 102
 Cibinel, A., Daddi, E., Sargent, M. T., et al. 2019, *MNRAS*, 485, 5631
 Ciesla, L., Buat, V., Boquien, M., et al. 2021, *A&A*, 653, A6
 Conroy, C., & Gunn, J. E. 2010, *ApJ*, 712, 833
 Conroy, C., Gunn, J. E., & White, M. 2009, *ApJ*, 699, 486
 Cooray, A., Calanog, J., Wardlow, J. L., et al. 2014, *ApJ*, 790, 40
 Cox, T. J., Jonsson, P., Somerville, R. S., Primack, J. R., & Dekel, A. 2008, *MNRAS*, 384, 386
 Crain, R. A., Schaye, J., Bower, R. G., et al. 2015, *MNRAS*, 450, 1937
 Davé, R., Anglés-Alcázar, D., Narayanan, D., et al. 2019, *MNRAS*, 486, 2827
 Davé, R., Finlator, K., Oppenheimer, B. D., et al. 2010, *MNRAS*, 404, 1355
 Dayal, P., Ferrara, A., Sommovigo, L., et al. 2022, *MNRAS*, 512, 989
 Dekel, A., Sari, R., & Ceverino, D. 2009, *ApJ*, 703, 785
 Devriendt, J. E. G., & Guiderdoni, B. 2000, *A&A*, 363, 851
 Di Cesare, C., Graziani, L., Schneider, R., et al. 2023, *MNRAS*, 519, 4632
 Di Matteo, P., Combes, F., Melchior, A. L., & Semelin, B. 2007, *A&A*, 468, 61
 Dotter, A. 2016, *ApJS*, 222, 8
 Draine, B. T. 2003, *ARA&A*, 41, 241
 Draine, B. T., & Li, A. 2007, *ApJ*, 657, 810
 Dudzevičiūtė, U., Smail, I., Swinbank, A. M., et al. 2021, *MNRAS*, 500, 942
 Duncan, K., Conselice, C. J., Mundy, C., et al. 2019, *ApJ*, 876, 110
 Dwek, E. 1998, *ApJ*, 501, 643
 Endsley, R., Stark, D. P., Lyu, J., et al. 2022, *MNRAS*, 520, 4609
 Fensch, J., Renaud, F., Bournaud, F., et al. 2016, *MNRAS*, 465, 1934
 Ferrara, A., Sommovigo, L., Dayal, P., et al. 2022, *MNRAS*, 512, 58
 Ferrarotti, A. S., & Gail, H. P. 2006, *A&A*, 447, 553
 Finlator, K., Davé, R., Papovich, C., & Hernquist, L. 2006, *ApJ*, 639, 672
 Flores Velázquez, J. A., Gurvich, A. B., Faucher-Giguère, C.-A., et al. 2021, *MNRAS*, 501, 4812
 Fontanot, F., Monaco, P., Silva, L., & Grazian, A. 2007, *MNRAS*, 382, 903
 Fudamoto, Y., Oesch, P. A., Schouws, S., et al. 2021, *Natur*, 597, 489
 Geach, J. E., Dunlop, J. S., Halpern, M., et al. 2017, *MNRAS*, 465, 1789
 Ginolfi, M., Graziani, L., Schneider, R., et al. 2018, *MNRAS*, 473, 4538
 Ginolfi, M., Schneider, R., Valiante, R., et al. 2019, *MNRAS*, 483, 1256
 Granato, G. L., De Zotti, G., Silva, L., Bressan, A., & Danese, L. 2004, *ApJ*, 600, 580
 Granato, G. L., Ragone-Figueroa, C., Taverna, A., et al. 2021, *MNRAS*, 503, 511
 Graziani, L., Schneider, R., Ginolfi, M., et al. 2020, *MNRAS*, 494, 1071
 Guiderdoni, B., Hivon, E., Bouchet, F. R., & Maffei, B. 1998, *MNRAS*, 295, 877
 Hahn, O., & Abel, T. 2011, *MNRAS*, 415, 2101
 Hashimoto, T., Inoue, A. K., Mawatari, K., et al. 2019, *PASJ*, 71, 71
 Hayward, C. C., Behroozi, P. S., Somerville, R. S., et al. 2013a, *MNRAS*, 434, 2572
 Hayward, C. C., Chapman, S. C., Steidel, C. C., et al. 2018, *MNRAS*, 476, 2278
 Hayward, C. C., Kereš, D., Jonsson, P., et al. 2011, *ApJ*, 743, 159
 Hayward, C. C., Lanz, L., Ashby, M. L. N., et al. 2014, *MNRAS*, 445, 1598
 Hayward, C. C., Narayanan, D., Kereš, D., et al. 2013b, *MNRAS*, 428, 2529
 Hodge, J. A., Karim, A., Smail, I., et al. 2013, *ApJ*, 768, 91
 Hopkins, P. F. 2015, *MNRAS*, 450, 53
 Hopkins, P. F., Gurvich, A. B., Shen, X., et al. 2023, arXiv:2301.08263
 Hopkins, P. F., Hernquist, L., Cox, T. J., & Kereš, D. 2008, *ApJS*, 175, 356
 Hopkins, P. F., Kereš, D., Oñorbe, J., et al. 2014, *MNRAS*, 445, 581
 Hughes, D. H., Serjeant, S., Dunlop, J., et al. 1998, *Natur*, 394, 241
 Hutter, A., Dayal, P., Yepes, G., et al. 2021, *MNRAS*, 503, 3698
 Ivison, R. J., Lewis, A. J. R., Weiss, A., et al. 2016, *ApJ*, 832, 78
 Iwamoto, K., Brachwitz, F., Nomoto, K., et al. 1999, *ApJS*, 125, 439
 Iyer, K. G., Gawiser, E., Faber, S. M., et al. 2019, *ApJ*, 879, 116
 Iyer, K. G., Tacchella, S., Genel, S., et al. 2020, *MNRAS*, 498, 430
 Karim, A., Swinbank, A. M., Hodge, J. A., et al. 2013, *MNRAS*, 432, 2
 Kartaltepe, J. S., Sanders, D. B., Le Floc'h, E., et al. 2010, *ApJ*, 721, 98
 Kaviraj, S., Cohen, S., Windhorst, R. A., et al. 2013, *MNRAS*, 429, L40
 Kennicutt, R. C. J. 1989, *ApJ*, 344, 685
 Kim, J.-h., Wise, J. H., Abel, T., et al. 2019, *ApJ*, 887, 120
 Knudsen, K. K., Watson, D., Frayer, D., et al. 2017, *MNRAS*, 466, 138
 Kroupa, P. 2002, *Sci*, 295, 82
 Krumholz, M. R., & Gnedin, N. Y. 2011, *ApJ*, 729, 36
 Lacey, C. G., Baugh, C. M., Frenk, C. S., et al. 2016, *MNRAS*, 462, 3854
 Lagos, C. d. P., Robotham, A. S. G., Trayford, J. W., et al. 2019, *MNRAS*, 489, 4196
 Laporte, N., Ellis, R. S., Boone, F., et al. 2017, *ApJL*, 837, L21
 Le Fèvre, O., Béthermin, M., Faisst, A., et al. 2020, *A&A*, 643, A1
 Leńniewska, A., & Michałowski, M. J. 2019, *A&A*, 624, L13
 Lewis, J. S. W., Ocvirk, P., Dubois, Y., et al. 2023, *MNRAS*, 519, 5987
 Li, Q., Narayanan, D., & Davé, R. 2019, *MNRAS*, 490, 1425
 Li, Q., Narayanan, D., Torrey, P., Davé, R., & Vogelsberger, M. 2021, *MNRAS*, 507, 548
 Lofthouse, E. K., Kaviraj, S., Conselice, C. J., Mortlock, A., & Hartley, W. 2017, *MNRAS*, 465, 2895
 Lovell, C. C., Geach, J. E., Davé, R., et al. 2021a, *MNRAS*, 515, 3644
 Lovell, C. C., Geach, J. E., Davé, R., Narayanan, D., & Li, Q. 2021b, *MNRAS*, 502, 772
 Lovell, C. C., Vijayan, A. P., Thomas, P. A., et al. 2021c, *MNRAS*, 500, 2127
 Lucy, L. B. 1999, *A&A*, 344, 282
 Ma, J., Gonzalez, A. H., Vieira, J. D., et al. 2016, *ApJ*, 832, 114
 Makiya, R., & Hirashita, H. 2022, *MNRAS*, 517, 2076
 Mancini, M., Schneider, R., Graziani, L., et al. 2015, *MNRAS*, 451, L70
 Marinacci, F., Sales, L. V., Vogelsberger, M., Torrey, P., & Springel, V. 2019, *MNRAS*, 489, 4233
 Marrone, D. P., Spilker, J. S., Hayward, C. C., et al. 2018, *Natur*, 553, 51
 Mathis, J. S., Rumpl, W., & Nordsieck, K. H. 1977, *ApJ*, 217, 425
 McAlpine, S., Helly, J. C., Schaller, M., et al. 2016, *A&C*, 15, 72
 McAlpine, S., Smail, I., Bower, R. G., et al. 2019, *MNRAS*, 488, 2440
 McKee, C. 1989, in Proc. IAU Symp. 135, Interstellar Dust, ed. L. J. Allamandola & A. G. M. Tielens (Dordrecht: Kluwer), 431
 McKinney, J., Hayward, C. C., Rosenthal, L. J., et al. 2021, *ApJ*, 921, 55
 McKinnon, R., Torrey, P., & Vogelsberger, M. 2016, *MNRAS*, 457, 3775
 McKinnon, R., Torrey, P., Vogelsberger, M., Hayward, C. C., & Marinacci, F. 2017, *MNRAS*, 468, 1505
 McKinney, W. 2010, in Proc. 9th Python in Science Conf. 445, ed. S. van der Walt & J. Millman, 56
 Michałowski, M. J. 2015, *A&A*, 577, A80
 Mihos, J. C., & Hernquist, L. 1994, *ApJL*, 431, L9
 Mihos, J. C., & Hernquist, L. 1996, *ApJ*, 464, 641
 Miller, T. B., Hayward, C. C., Chapman, S. C., & Behroozi, P. S. 2015, *MNRAS*, 452, 878
 Muratov, A. L., Kereš, D., Faucher-Giguère, C.-A., et al. 2015, *MNRAS*, 454, 2691
 Narayanan, D., Dey, A., Hayward, C. C., et al. 2010b, *MNRAS*, 407, 1701
 Narayanan, D., Hayward, C. C., Cox, T. J., et al. 2010a, *MNRAS*, 401, 1613

- Narayanan, D., Turk, M., Feldmann, R., et al. 2015, *Natur*, **525**, 496
- Narayanan, D., Turk, M. J., Robitaille, T., et al. 2020, *ApJS*, **252**, 12
- Narayanan, D., Turk, M. J., Robitaille, T., et al. 2021, *ApJS*, **252**, 12
- Nomoto, K., Tominaga, N., Umeda, H., Kobayashi, C., & Maeda, K. 2006, *NuPhA*, **777**, 424
- Oppenheimer, B. D., & Davé, R. 2006, *MNRAS*, **373**, 1265
- pandas development team 2020, Pandas v1.5.0, Zenodo, doi: [10.5281/zenodo.7093122](https://doi.org/10.5281/zenodo.7093122)
- Poole, G. B., Angel, P. W., Mutch, S. J., et al. 2016, *MNRAS*, **459**, 3025
- Popping, G., Somerville, R. S., & Galametz, M. 2017, *MNRAS*, **471**, 3152
- Rahmati, A., Pawlik, A. H., Raičević, M., & Schaye, J. 2013, *MNRAS*, **430**, 2427
- Segovia Otero, Á., Renaud, F., & Agertz, O. 2022, *MNRAS*, **516**, 2272
- Renaud, F., Agertz, O., Read, J. I., et al. 2021, *MNRAS*, **503**, 5846
- Reuter, C., Vieira, J. D., Spilker, J. S., et al. 2020, *ApJ*, **902**, 78
- Riechers, D. A., Bradford, C. M., Clements, D. L., et al. 2013, *Natur*, **496**, 329
- Robitaille, T. P. 2011, *A&A*, **536**, A79
- Robitaille, T. P., Churchwell, E., Benjamin, R. A., et al. 2012, *A&A*, **545**, A39
- Sales, L. V., Navarro, J. F., Theuns, T., et al. 2012, *MNRAS*, **423**, 1544
- Sánchez Almeida, J., Elmegreen, B. G., Muñoz-Tuñón, C., & Elmegreen, D. M. 2014, *A&ARv*, **22**, 71
- Sanders, D. B., & Mirabel, I. F. 1996, *ARA&A*, **34**, 749
- Sanders, D. B., Soifer, B. T., Elias, J. H., et al. 1988a, *ApJ*, **325**, 74
- Sanders, D. B., Soifer, B. T., Elias, J. H., Neugebauer, G., & Matthews, K. 1988b, *ApJL*, **328**, L35
- Schaller, M., Dalla Vecchia, C., Schaye, J., et al. 2015, *MNRAS*, **454**, 2277
- Schaye, J., Crain, R. A., Bower, R. G., et al. 2015, *MNRAS*, **446**, 521
- Schmidt, M. 1959, *ApJ*, **129**, 243
- Shimizu, I., Yoshida, N., & Okamoto, T. 2012, *MNRAS*, **427**, 2866
- Simpson, J. M., Swinbank, A. M., Smail, I., et al. 2014, *ApJ*, **788**, 125
- Smail, I., Ivison, R. J., & Blain, A. W. 1997, *ApJL*, **490**, L5
- Smith, B. D., Bryan, G. L., Glover, S. C. O., et al. 2017, *MNRAS*, **466**, 2217
- Somerville, R. S., Gilmore, R. C., Primack, J. R., & Domínguez, A. 2012, *MNRAS*, **423**, 1992
- Somerville, R. S., Primack, J. R., & Faber, S. M. 2001, *MNRAS*, **320**, 504
- Sommovigo, L., Ferrara, A., Pallottini, A., et al. 2022, *MNRAS*, **513**, 3122
- Sparre, M., & Springel, V. 2016, *MNRAS*, **462**, 2418
- Speagle, J. S., Steinhardt, C. L., Capak, P. L., & Silverman, J. D. 2014, *ApJS*, **214**, 15
- Spilker, J. S., Hayward, C. C., Marrone, D. P., et al. 2022, *ApJL*, **929**, L3
- Swinbank, A. M., Lacey, C. G., Smail, I., et al. 2008, *MNRAS*, **391**, 420
- Thompson, R. 2014, pyGadgetReader: GADGET snapshot reader for python, Astrophysics Source Code Library, ascl:[1411.001](https://ascl.net/1411.001)
- Toomre, A., & Toomre, J. 1972, *ApJ*, **178**, 623
- Topping, M. W., Stark, D. P., Endsley, R., et al. 2022, *MNRAS*, **516**, 975
- Triani, D. P., Sinha, M., Croton, D. J., Pacifici, C., & Dwek, E. 2020, *MNRAS*, **493**, 2490
- Trinca, A., Schneider, R., Valiante, R., et al. 2022, *MNRAS*, **511**, 616
- Turk, M. J., Smith, B. D., Oishi, J. S., et al. 2011, *ApJS*, **192**, 9
- Valiante, R., Schneider, R., Bianchi, S., & Andersen, A. C. 2009, *MNRAS*, **397**, 1661
- Valiante, R., Schneider, R., Salvadori, S., & Gallerani, S. 2014, *MNRAS*, **444**, 2442
- van de Voort, F., Schaye, J., Booth, C. M., Haas, M. R., & Dalla Vecchia, C. 2011, *MNRAS*, **414**, 2458
- van der Walt, S., Colbert, S. C., & Varoquaux, G. 2011, *CSE*, **13**, 22
- Vieira, J. D., Marrone, D. P., Chapman, S. C., et al. 2013, *Natur*, **495**, 344
- Vijayan, A. P., Lovell, C. C., Wilkins, S. M., et al. 2021, *MNRAS*, **501**, 3289
- Virtanen, P., Gommers, R., Oliphant, T. E., et al. 2020, *NatMe*, **17**, 261
- Wardlow, J. L., Smail, I., Coppin, K. E. K., et al. 2011, *MNRAS*, **415**, 1479
- Watson, D., Christensen, L., Knudsen, K. K., et al. 2015, *Natur*, **519**, 327
- Weingartner, J. C., & Draine, B. T. 2001, *ApJ*, **548**, 296
- Wilkins, S. M., Vijayan, A. P., Lovell, C. C., et al. 2022, *MNRAS*, **517**, 3227
- Zavala, J. A., Casey, C. M., Manning, S. M., et al. 2021, *ApJ*, **909**, 165
- Zavala, J. A., Casey, C. M., Spilker, J., et al. 2022, *ApJ*, **933**, 242
- Zavala, J. A., Montaña, A., Hughes, D. H., et al. 2018, *NatAs*, **2**, 56